Ingrid Midtbust Hjelle

Study of the Damage Potential of the FCC-ee Beams

TFY4510 - Physics, Specialization project
Supervisor: Assoc. Prof. Jon Andreas Støvneng
External supervisor: Dr. Christoph Wiesner
Autumn 2024

Norwegian University of Science and Technology
Faculty of Natural Sciences
Department of Physics

NTNU

European Organization for Nuclear Research
Machine Protection and Electrical Integrity Group
Control and Beam Studies for Protection

CERN

CERN-THESIS-2024-357
03/02/2025

ACKNOWLEDGMENTS

I want to express my gratitude to everyone who has supported me during this project. First and foremost, I wish to thank my supervisor, Dr. Christoph Wiesner, for invaluable guidance and expertise, both during my time at CERN and while writing this report.

I would also like to thank Audrey Piccini, Dr. Federico Carra, Dr. Michele Pasquali, and Dr. Anton Lechner for their valuable contributions and insightful discussions on the analysis and results, David Gancarcik, Cedric Hernalsteens, and Milosz Blaszkiewicz for their support in ensuring the efficient use of computational resources, and Jens Kruse-Hansen, Inken Kolthoff, Silvio Rasile, and Jeppe Don for their crucial contributions to the scripts and simulation setup.

Lastly, I want to express my gratitude to Dr. Daniel Wollmann for the opportunity to work on this project within his section, and for his support throughout the process.

ABSTRACT

The beam characteristics of the Future Circular Collider electron-positron (FCC-ee) beam differ vastly from those of the Large Hadron Collider (LHC) beam and the High Luminosity LHC (HL-LHC) beam, presenting new challenges for assessing beam impact and damage potential. The FCC-ee consist of electrons with significantly lower energies than the protons in the LHC and HL-LHC beams. In the Z mode, the total stored beam energy will be 17.5 MJ, while the same values for the LHC and HL-LHC beams are 362 MJ and 681 MJ, respectively. The FCC-ee beams will also operate with a highly asymmetric emittance ($\epsilon_x > \epsilon_y$), while the LHC and HL-LHC beams can be approximated as round.

This report presents the stored beam energy and analytical estimations for the energy density of the FCC-ee beams, considering a range of beam sizes, and compares them with the LHC and HL-LHC beams. Then, energy deposition of the generic scenario of a direct beam impact on a graphite target with nominal material density is simulated using FLUKA. Results show that the peak energy depositions for the FCC-ee beams with Z mode parameters are comparable to those of the LHC and HL-LHC beams. However, the shape of the energy deposition shower is more peaked and localized close to the beam impact point.

In the last step, the hydrodynamic response of the material due to the impact of a round beam with a corresponding peak energy deposition is analyzed. After the impact of five bunches, it is observed a maximum energy deposition and temperature rise comparable to those due to the impact of the HL-LHC beam with a beam size of $\sigma = 0.5$ mm. However, the local target density depletes more rapidly.

CONTENTS

Chapter 1

INTRODUCTION

The European Organization for Nuclear Research (CERN) is a leading institution for particle physics research that studies fundamental questions about elementary particles, antimatter, dark matter, the spatial dimensions of space, and more [1]. CERN studies a Future Circular Collider (FCC) [2] as part of its long-term strategy. The project would consist of two stages: an electron/positron collider (FCC-ee) and then a hadron collider (FCC-hh). The FCC-ee collider will study Z, W, Higgs and $t\bar{t}$ production.

To safely operate such a collider, it is crucial to design an appropriate machine protection system [3]. This relies on understanding the damage potential of the FCC-ee beams. Using FLUKA [4–7], an energy deposition code, and ANSYS Autodyn [8], a hydrodynamic code, this project studies the impact of the FCC-ee beam on a graphite target. The focus will be on the Z mode of the FCC-ee collider, which has the highest machine protection criticality.

The Z mode of the FCC-ee collider will operate at a particle energy of 45.6 GeV and with a bunch intensity of 2.14×10^{11} e^-/e^+ [9], which results in a total stored beam energy of 17.5 MJ. In comparison, the beams of the Large Hadron Collider (LHC) [10] and the High Luminosity LHC (HL-LHC) [11] have a particle energy of 7000 GeV and a bunch intensity of 1.15×10^{11} p^+ and 2.2×10^{11} p^+, respectively, resulting in stored beam energies of 362 MJ and 681 MJ, respectively.

The FCC-ee beams have very different beam characteristics than the LHC and HL-LHC beams. The transverse beam emittance is significantly smaller in the vertical plane than in the horizontal ($\epsilon_y < \epsilon_x$) [9]. In addition, high-energy electrons interact with the material and thus deposit energy differently than high-energy protons [12].

The damage potential for the worst-case scenario of a direct beam impact has been previously studied for the LHC beam [13–18] and HL-LHC beam [19, 20]. It is now of interest to study a similar scenario for the FCC-ee beam and compare the results.

I would like to specifically highlight a previous LHC beam impact study [17, 18], which simulated the impact of the full LHC beam with a beam size of 0.5 mm. As a prerequisite to this study, a lot of work was conducted to set up a simulation framework that is also used as a base for this study [21, 22]. In addition, the data from this study is used to compare the FCC-ee results with the LHC beam.

This project report is structured as follows: Chapter 2 provides relevant background information, including introducing the FCC-ee project, machine protection, and particle-

matter interactions. Chapter 3 gives an overview of the simulation tools FLUKA and ANSYS Autodyn. Chapter 4 presents and analyses the damage potential of the FCC-ee beams, including analytic estimations and simulation results of the energy distribution in a graphite target. Chapter 5 presents initial hydrodynamic simulations for the impact of the first five bunches of an approximated round FCC-ee beam. Finally, the main conclusions and an outlook are given in Chapter 6.

Chapter 2

BACKGROUND

The Large Hadron Collider (LHC) [10] at The European Organization for Nuclear Research (CERN) has been transformative for particle physics, providing insights that reshaped our understanding of the universe — from confirming the existence of the Higgs boson to pushing the limits of our knowledge about fundamental particles and forces [1]. With the upgrade to the High Luminosity LHC (HL-LHC) [11], the luminosity will almost double, allowing experiments at CERN to obtain more data from rare collisions.

The 2020 Update of the European Strategy for Particle Physics [23] stated that the top priority for the next collider should be an electron-positron Higgs factory. In the long term, the European particle physics community plans for a proton-proton collider capable of reaching a center-of-mass energy of approximately 100 TeV. The Future Circular Collider (FCC) would use a 91 km [9, p.3] long tunnel that will be located in the Geneva region. Figure 2.0.1 shows an aerial view of the proposed size and location.

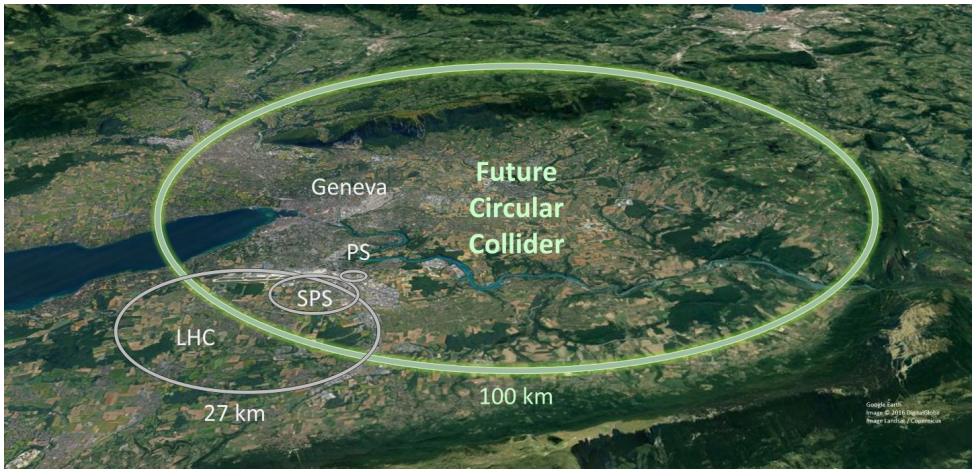

Figure 2.0.1: Aerial view of the proposed FCC tunnel [24].

The FCC is proposed to have two stages [2]. The first stage is an electron-positron collider, named the Future Circular electron-positron Collider, FCC-ee, designed as a high-precision instrument that offers direct and indirect sensitivity to new physics [25, p.11]. The next stage is a hadron collider, the Future Circular hadron-hadron Collider, FCC-hh, which is set to be built in the same tunnel as the FCC-ee. The goal of this collider is to achieve a center-of-mass energy of 100 TeV, which could directly produce new particles up to several tens of TeV and measure the Higgs self-coupling [25, p.11].

2.1 Future Circular electron-positron Collider

This project will study the damage potential of FCC-ee beams. This section will present and discuss the relevant aspects of FCC-ee.

The aim of the FCC-ee is to study Z, W, Higgs and $t\bar{t}$ production with very high precision [25, p.11]. It will be a Higgs, electroweak and top factory with high luminosity [2]. Table 2.1.1 presents some main parameters for these four operational modes. The bunch intensity is calculated from the beam current in [9].

Table 2.1.1: Preliminary key parameters for the different FCC-ee modes [9]

Running mode	**Z**	**W**	**ZH**	**$t\bar{t}$**
Particle Energy [GeV]	45.6	80	120	182.5
Number of Bunches	11200	1780	440	60
Bunch Intensity [10^{11}]	2.14	1.45	1.32	1.55
Stored Beam Energy [MJ]	17.5	3.3	1.1	0.3
Horizontal Emittance ϵ_x [nm]	0.71	2.17	0.71	1.59
Vertical Emittance ϵ_y [pm]	1.9	2.2	1.4	1.6

The first row in Table 2.1.1 presents the particle energy in each operational mode. For head-on collisions, the center-of-mass energy will be twice the particle energy. To produce a particular particle in a collision, the center-of-mass energy, typically referred to as $\sqrt{s}$, has to be at least equal to the mass-energy of that particle. In the Higgs running mode, ZH, the production of Higgs bosons happens mainly through the Higgsstrahlung process, $e^+e^- \rightarrow HZ$, and WW fusion, $e^+e^- \rightarrow (WW \rightarrow H)\ \nu\bar{\nu}$ [25, p.45]. A center of mass energy of 240 GeV yields the highest event rate per unit time. At this energy, the production of the Higgs boson happens almost exclusively by the Higgsstrahlung process. Hence this operational mode is called ZH.

This project will focus on the Z mode, as this mode has the highest damage potential. Even if this mode has the smallest particle energy of 45.6 GeV, it has a significantly higher stored beam energy of 17.5 MJ. This is a result of its high number of bunches and high bunch intensity, two critical factors to consider from a machine protection perspective. Comparing, for example, with the $t\bar{t}$ mode, the particle energy is 4 times as high as in the Z mode. However, the total number of particles is 9.3×10^{12}, compared to the 2.4×10^{15} particles in the Z mode. Thus, in the worst-case scenario of the loss of the full FCC-ee beam, the Z mode will have the highest expected damage.

2.2 Machine Protection

With a stored beam energy of 17.5 MJ, an uncontrolled release of even a small fraction of this energy could damage accelerator equipment. Therefore, an appropriate machine protection system is required. To design such a system, a thorough understanding of failure cases and consequences is needed [3].

Due to the high amount of stored beam energy and the complexity of the hardware systems, it is not excluded that failure cases beyond what the machine protection system is designed for can occur. These are referred to as beyond-design failure cases. Understanding the causes and consequences of these failure cases is crucial for designing the machine protection system. In particular, it is essential to understand the consequences of beam impact events, specifically what happens when the beam impacts various components directly.

A worst-case scenario is the loss of the full beam at a single point. With a particle energy of 45.6 GeV, an impact like this will result in significant damage. The FCC-ee beam poses specific challenges because the beam is strongly asymmetric in the horizontal and vertical planes, and the beam size is significantly smaller than, for example, the LHC beams.

2.2.1 Loss of the Full Beam at a Single Point

Figure 2.2.1 shows a schematic of a direct impact at a single point of the FCC-ee beam. The figure is not to scale.

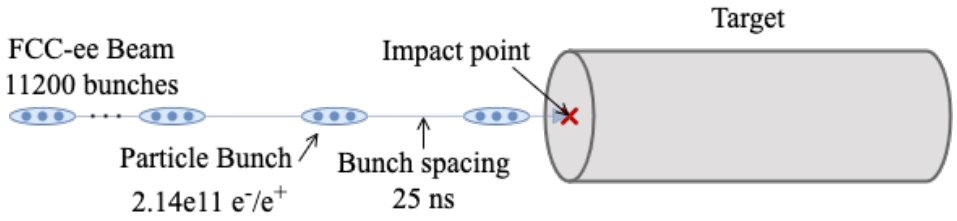

Figure 2.2.1: Illustration of the loss of the full FCC-ee beam at a single point.

This failure has been studied extensively for the LHC beam [13–18], and the methods have been applied to HL-LHC parameters [20]. These studies have found that the penetration depth of the full beam increases significantly due to a phenomenon called hydrodynamic tunneling. As the high-energy proton bunches impact the target, they create high pressure and temperature, which in turn depletes the material density along the beam path. When successive proton bunches impact at a later point, they will thus impact on a target with lower density, and as a result, the energy will be deposited further

into the material.

The hydrodynamic tunneling phenomena was experimentally verified at the CERN High Radiation to Materials (HiRadMat) Facility [26] using the SPS beam (450 GeV, 3.4×10^{13} p^+) impacting on a cylindrical copper target [14]. In addition to proving the existence of the phenomena, the results of the experiment aligned well with simulations. This is a crucial result, given that conducting a similar experiment at higher energies is practically very challenging.

Understanding what happens in this extreme scenario is relevant to the machine protection design and for understanding the behavior of the high-energy particles. The following section will consider the basics of particle-matter interactions, providing a foundation for understanding the consequences of a full beam impact.

2.3 Particle-Matter Interactions

All particles in the beam and any secondary particles they produce will interact with the material they impact [12]. The type of interaction depends on the energy of each particle. Leptons lose energy primarily through two mechanisms: at low energies, they have Coulomb interactions with atomic electrons, causing ionization, while at energies above a critical energy, they lose energy by emitting photons in the electrostatic field of a nucleus, a process known as bremsstrahlung [27, p.18]. Hadrons also dissipate energy through inelastic nuclear collisions if the energy is of the order of GeV or higher [27, p.21]. If the energy of the incident hadron is high enough, these collisions can result in the production of new particles. In addition, hadrons lose energy continuously through ionization, and these Coulomb interactions are much more frequent than nuclear collisions.

Charges particles that transverse through the material will also experience Coulomb scattering with atomic nuclei [12]. This is a small-angle deflection that affects the path of the particle. Lighter particles scatter more than heavier ones, meaning that protons are more likely to have a more straight path through the material than electrons. However, at higher energies, electrons are increasingly affected by Bremsstrahlung processes, and this will, in turn, minimize the scattering effects on the path.

2.3.1 Particle Showers

When a high-energy electron radiates a bremsstrahlung photon, this photon can, in turn, produce an e^+e^- pair through pair-production [27, p.19]. This forms a cycle of photon emission and pair production that can repeat multiple times, resulting in an electromagnetic shower. The shower develops as long as the particle energies remain above a critical energy threshold. Below this threshold, ionization losses dominate, gradually halting the

cascade.

A similar process happens for high-energy hadrons. As hadrons interact with matter, secondary particles are produced, which will continue interacting with the material further downstream [27, p.21]. This creates a hadronic shower. Unlike electromagnetic showers, which develop in a relatively uniform manner, hadronic showers are highly variable due to the diverse types of particles and interactions involved. Furthermore, any produced π^0 will instantaneously decay as $\pi^0 \rightarrow \gamma\gamma$, causing an electromagnetic shower within the hadronic one. In addition, about 30% of energy in hadronic showers is not detectable as it is lost due to nuclear excitation and break up [27, p.21].

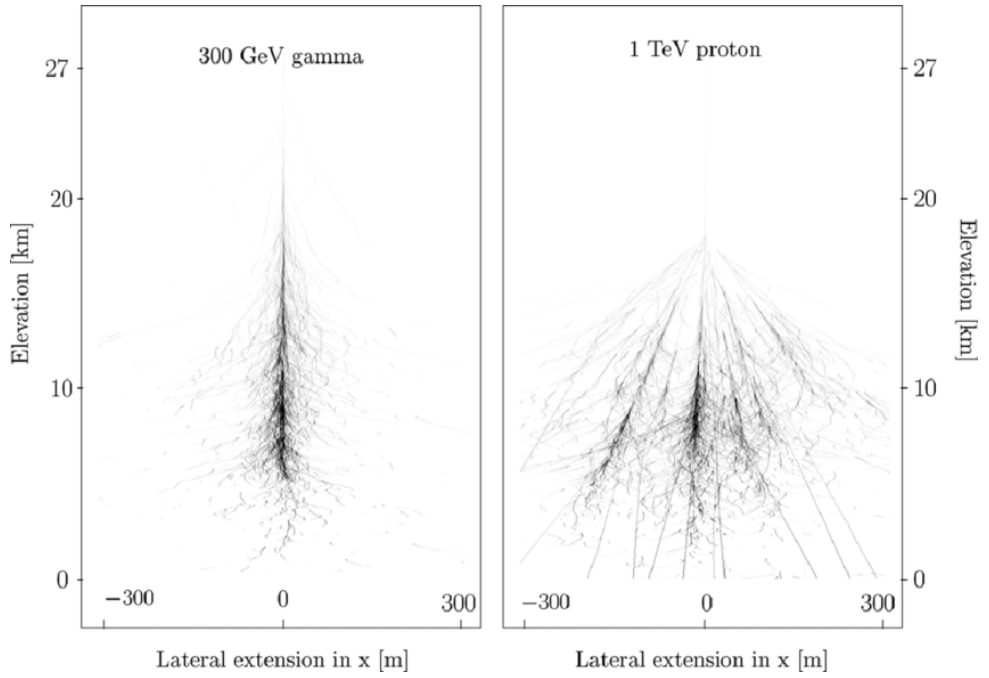

Figure 2.3.1: The difference in the evolution of an electromagnetic shower, simulated from a 300 GeV γ-ray, and a hadronic cascade, simulated from a 1 TeV proton [28, p.12].

Figure 2.3.1 illustrates the different electromagnetic and hadronic shower patterns. Electromagnetic showers spread out more uniformly, and most of the energy is located along the beam path. On the other hand, the hadronic shower spreads out more irregularly. Another important difference that can be clearly seen in Fig. 2.3.1 is how the electromagnetic shower has stray electrons deviating from the beam path right away, whilst the protons move in a straight line before the irregular patter occur.

2.3.2 Dynamic Response of the Material

In addition to understanding how the particles interact with matter, an equally important part is understanding the material's dynamic response. The different types of responses depend on the amount and distribution of the deposited energy and the time scale over

which it is deposited [29]. On the one hand, for cases with low deposited energy occurring over a relatively long timescale, the structural response can be reduced to a steady-state problem. On the other hand, if the deposited energy is extremely high and happens over only a few milliseconds or less, extreme conditions can be reached. The material can experience a thermal shock due to thermal expansion being partly prevented by inertia, which in turn can create dynamic stresses that propagate through the material at the velocity of sound. Figure 2.3.2 gives an overview of the different types of material responses.

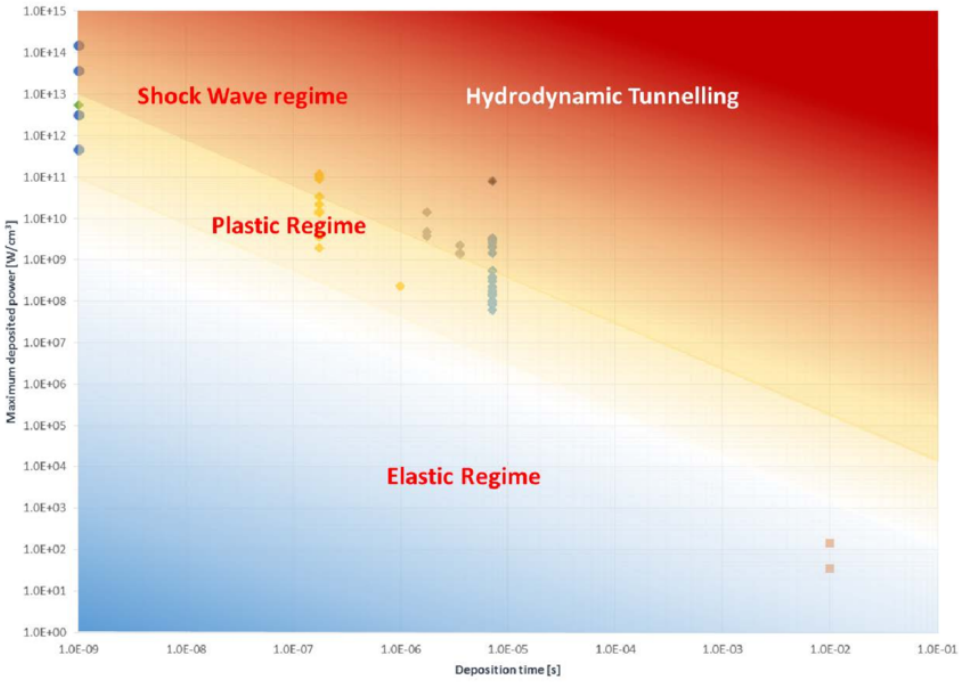

Figure 2.3.2: The difference categories of material response, illustrated based on the amount of deposited power over time [29].

Responses within the elastic regime do not cause permanent changes to the material, i.e the material returns to its original state once the applied stress is no longer applies [29]. As the energy deposition increases, the material enters the plastics regime. Here, localized deformations can occur as stress waves exceed the elastic limits of the material. At even higher energy levels, the material reaches the shock wave regime, where the stress waves are sufficiently strong to cause substantial material damage.

The last regime, hydrodynamic tunneling, was briefly mentioned in Section 2.2.1. Significant material density depletion happens simultaneously with the beam impact, causing the secondary showers to penetrate deeper into the material. Figure 2.3.2 illustrates how this regime is reached when there is a high amount of energy deposited in the material over longer timescales ($>\mu$s).

Chapter 3

SIMULATION METHOD

Simulating the interactions of high-energy particles with materials is a complex and computationally intensive task, requiring specialized tools to accurately model both particle behavior and the resulting material response. In this thesis, two simulation tools were employed to address these challenges: FLUKA [4–7], a Monte Carlo code for particle transport and energy deposition, and ANSYS Autodyn [8], a hydrodynamic code for dynamic structural simulations. This chapter introduces these tools, outlining their key features and roles in studying the impact of the FCC-ee beams on target materials.

3.1 FLUKA

FLUKA is a multipurpose multiparticle Monte Carlo code that simulates the interaction and transport of hadrons, heavy ions, and electromagnetic particles [5, p.3]. By implementing a range of physical models, enforcing conservation laws, and validating the results against experimental data when possible, FLUKA provides predictions with minimal free parameters. With its high accuracy and ability to handle complex geometries, FLUKA is useful in a wide range of applications, such as particle detector studies, cosmic ray physics, radiotherapy, and much more.

3.1.1 The Monte Carlo Technique

The transport of particles is described by the interaction cross sections, which are based on probabilities [30]. The Monte Carlo technique is a stochastic method used to simulate particles and track them in arbitrary geometries. FLUKA uses pseudo-random numbers, which means that it uses an algorithm to determine numbers that appear to be randomly selected. When running a simulation, the initial state of the number generator is set as input. This state is referred to as the seed, and one specific seed will always refer to the same state, which is crucial for reproducibility [5, p.186]. This random sampling technique is the basis of the Monte Carlo technique. As a particle is transported through matter, the outcome of interactions is decided randomly at each step. This also holds for all secondary particles.

Before a FLUKA simulation, the user decides on how many particle histories will be simulated, referred to as the number of primaries [5, p.51]. All resulting secondary

particles are also simulated for each particle before moving on to a new one. This relies on two important assumptions utilized in FLUKA: that particles do not interact with each other and that material properties are unaffected by previous particles, i.e. particle transport can be simulated as a Markovian process [30, p.124]. In short, the fate of the particle is only dependent on the initial conditions of both the particle and the material.

The statistical accuracy of the results obtained from a Monte Carlo simulation depends on the number of particle histories run [30, p.124]. When running a FLUKA simulation, two important input parameters are the number of primaries n and the number of cycles N, representing the number of independent sets of simulations performed. The total number of simulated particles n_{tot} will be the product $n \cdot N$. A larger sample size will provide a lower statistical error, but it will also come with the cost of a higher computational time. The statistical uncertainty will scale according to Eq. 3.1 [30, p.120].

$$\sigma \propto \frac{1}{\sqrt{n_{\text{tot}}}} \tag{3.1}$$

3.1.2 Geometry and Material Definitions

The target in FLUKA is defined by creating geometry regions and filling them with either homogeneous material, vacuum, or "blackhole", a material that terminates particles that reach it [5, p.16]. For impact studies, the primary particles are defined to start their trajectory outside of the target. When this is the case, defining a region of vacuum surrounding the material is useful. FLUKA then requires that the target and the vacuum are surrounded by a region of "blackhole" [5, p.15]. Figure 3.1.1 presents an example of a cylindrical target defined in FLUKA [16–18, 22].

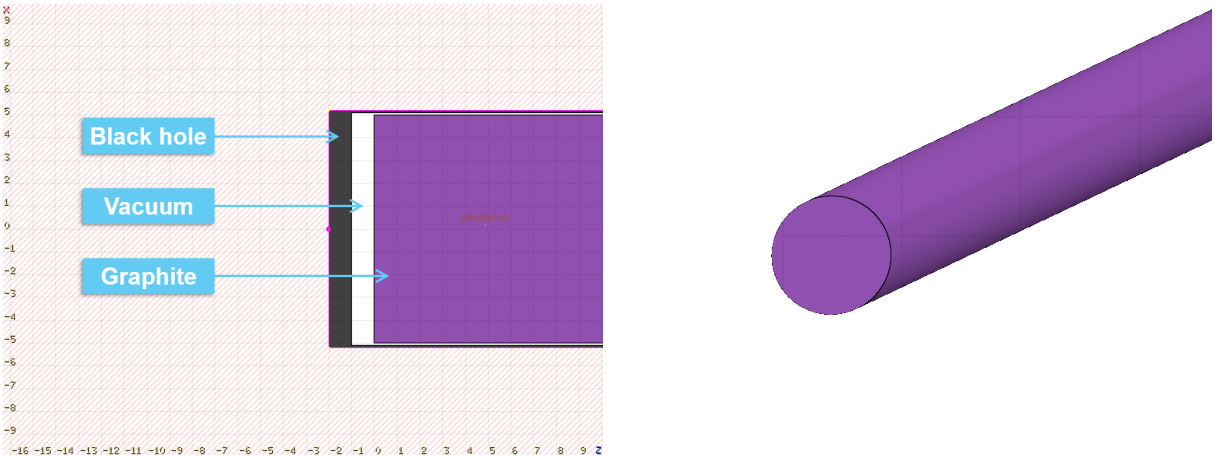

(a) Cross-sectional view (2D) of the zx plane. **(b)** 3D view.

Figure 3.1.1: Example of a cylindrical target defined in FLUKA.

3.1.3 Running FLUKA Simulations

The most efficient way of running a FLUKA simulation is by using parallel computing. Each simulation is computationally expensive, so having access to multiple CPUs can significantly reduce the computational time. For this project, I used the HTCondor cluster [31], a cluster that allows a high number of jobs to be run simultaneously. When setting up the study, an important task is to find a combination of the number of jobs and the number of primaries in each job that yields a low enough statistical error and has a low enough runtime. Multiple other factors also affected the runtime, such as the particle type and the complexity of the simulated geometry. So, the combination of a number of primaries and jobs had to be tested and decided for each simulation setup.

3.1.4 FLUKA Output

To format the FLUKA output, this study uses the option USRBIN, a versatile scoring card designed to record various physical quantities within a defined region of the simulation geometry [5, p.57]. It allows users to monitor parameters such as energy deposition, particle fluence, and dose distributions. The scoring region can be specified in different coordinate systems (Cartesian, cylindrical, or spherical) and divided into bins to achieve the desired spatial resolution.

More specifically, this study used the DOSE option, which yields the energy output in units of GeV/g/particle. For the coordinate system, this project uses a Cartesian and a cylindrical one, depending on whether the problem is symmetrical. Both the used coordinate system and the binning will be specified in later sections when used.

3.2 ANSYS Autodyn

The Autodyn simulations used in this study are set up and performed by Audrey Piccini and Federico Carra [32]. The author conducts the data analysis.

The impact of high-energy beams at a single point is expected to result in heating and pressure waves, induce phase transitions in the material, and potentially even displacement of some material. These changes will happen rapidly, and while most of the damage is expected to occur locally close to the beam impact, the pressure waves travel further [33]. A simulation tool capable of handling such rapid and nonlinear changes is essential to capture these fast, localized dynamics accurately.

ANSYS Autodyn [8], a Finite Element Method (FEM) Tool, utilizes explicit time-integration schemes to efficiently simulate these highly dynamic events [33]. It takes the dose distribution simulated by FLUKA as input and uses it to simulate the hydrodynamic response of the material.

Table 3.2.1 presents the main simulation parameters used in this study.

Table 3.2.1: Main Autodyn Simulation Parameters

Equation of State	Tabular (SESAME)
Strength and Failure Model	none
Mesh	Eulerian

The SESAME library provides a tabular equation of state that can express strong nonlinearities and discontinuities in the material [17]. Studies conducted for the LHC beam [13–18] and the HL-LHC beam [20] found pressures in the order of GPa, which suggests that the hydrostatic response of the material will dominate over the deviatoric stress. In addition, the fracture mechanisms of the material are not of interest in these studies. Thus, neither the strength nor failure models have to be included.

Finally, the simulations use an Eulerian mesh. This mesh remains fixed in space while material flows through it. Another option is the Lagrangian mesh, where the mesh moves and deforms with the material. This mesh can provide a high accuracy when it comes to tracking material, however the Eulerian mesh has the advantage that it avoids element distortion. This is particularly important for this study, as it simplifies the interaction between Autodyn and FLUKA, making the simulation more robust and less prone to numerical errors.

Chapter 4

FCC-ee DAMAGE POTENTIAL

This chapter presents the results of the first phase of this study, which aims to establish a general understanding of the damage potential of the FCC-ee beam through analytic calculations and FLUKA simulations. By varying the beam size, the energy density and energy deposition are evaluated for various beam impact scenarios. The results are compared to those of the LHC and HL-LHC beams.

4.1 Analytic Estimations

The FCC-ee beam has very different characteristics than the LHC and HL-LHC beams. Table 4.1.1 compares the main parameters of the three beams. The total stored beam energy is given by the product of the particle energy and the total number of particles.

Table 4.1.1: Comparison of the Main Parameters for the FCC-ee Beam (Z mode) [9, p.3], and the Nominal Parameters for the LHC Beam [10, p.3] as well as the HL-LHC Beam [11, p.18].

	FCC-ee	**LHC**	**HL-LHC**
Particle Type	Electron/Positron	Proton	
Particle Energy [GeV]	45.6	7000	
Number of Bunches	11200	2808	2760
Number of Particles per Bunch [10^{11}]	2.14	1.15	2.2
Total Number of Particles [10^{15}]	2.4	0.32	0.61
Total Stored Beam Energy [MJ]	17.5	362	681

Table 4.1.1 shows that the FCC-ee beam's total stored energy is significantly lower than the values reached for both the LHC and HL-LHC beams, a direct consequence of the lower particle energy in the FCC-ee beam. However, assessing the damage potential requires considering not only the stored beam energy but also the beam size and particle type.

The FCC-ee beam's transverse size is much smaller than that of the LHC and HL-LHC beams. In particular, the FCC-ee beam has a significantly smaller emittance in the y-plane than in the x-plane, making it a flat beam. Both these characteristics will play a crucial role when studying the impact of the beam. In addition, as discussed in Section 2.3,

electrons and protons behave differently when interacting with material. Understanding this behavior is not possible through only analytic calculations. Therefore, the energy deposition pattern is simulated using FLUKA (Section 4.2).

This section presents the analytical estimations for the transverse beam size and energy density. The goal is to establish a foundational understanding of how the FCC-ee beams behaves in terms of beam dynamics and energy density, setting the stage for more detailed simulations and analyses in subsequent sections.

4.1.1 Theoretical Background

The transverse size of the beam, which typically is what is referred to as the beam size, is a measure of how particles are distributed spatially within the beam [34, ch.3.2.4]. It is commonly described using a Gaussian distribution, with the root-mean-square (rms) beam size, σ_{rms}, representing the standard deviation of the distribution. The beam size is determined by the emittance, ϵ, which is the phase space area occupied by the beam, and the beta-function, β, which is determined by the focusing mechanisms of the accelerator [35, p.9]. These are related by Eq. 4.1 [10, p.13].

$$\sigma_{\text{rms}} = \sqrt{\epsilon\beta} \tag{4.1}$$

For proton beams[1], the emittance decreases as the beam energy increases [34, p.85]. In high-energy accelerators, emittances are therefore often expressed in a normalized form, ϵ_{norm}, which accounts for relativistic effects. It is related to ϵ by Eq. 4.2 [10, p.13].

$$\epsilon_{\text{norm}} = \beta\gamma\epsilon \approx \gamma\epsilon \tag{4.2}$$

For ultra-relativistic particles with velocities close to the speed of light, $\beta \approx 1$ is a valid approximation. In Eq. 4.2, γ is the Lorentz factor, which accounts for the relativistic effects and is calculated as the ratio of the particle's total energy to its rest energy.

The emittances for the LHC and HL-LHC beams are typically given in the normalized form. So, to estimate their rms beam size, the first step is to calculate the unnormalized emittances. The Lorentz factor is calculated by Eq. 4.3 [27, p. 36].

$$\gamma = \frac{E_{\text{total}}}{E_{\text{rest}}} = \frac{E_{\text{kin}} + m_p c^2}{m_p c^2} \approx \frac{E_{\text{kin}}}{m_p c^2} \tag{4.3}$$

Here, the constant term 1 is neglected because the beam operates at energies much higher than the proton's rest energy. Table 4.1.2 presents the results of the calculations, where the value for the proton rest energy is taken from [36].

[1]Minor clarification added compared to the original version submitted to the Norwegian University of Science and Technology on 17.12.2024.

Table 4.1.2: Transverse Beam Emittances for the LHC Beam [10, p.3] and HL-LHC Beam [11, p.18]

	LHC	**HL-LHC**
Normalized Emittance [μm]	3.75	2.5
Particle Energy [GeV]	7000	
Proton Rest Energy [MeV/c^2]	938.27	
Emittance [pm]	503	335

4.1.2 Beam Size Calculations

The rms emittances for the FCC-ee in the Booster [37, p.361] and Collider [9, p.3] modes are presented in Table 4.1.3. Here, the Booster mode represents where the beams are being accelerated to the desired energy, whilst the Collider mode is, as the name suggests, where the beams are to collide.

As the β-function varies throughout the accelerator ring, the beam size is calculated for a range of β-function values. For the FCC-ee ring, the arc cells in the Z mode will have a β-function that varies between 30 m and 90 m [37, p.362]. At the beam dump, the β-function will be increased to as high as a few kilometers, so therefore, the value $\beta = 1000$ m is included as a reference.

Table 4.1.3 presents the beam size calculations for the chosen range of β-function values.

Table 4.1.3: Calculation of Beam Sizes for the FCC-ee (Booster and Collider Intensities) [9], LHC [10] and HL-LHC [11] Beams

	FCC-ee Booster		**FCC-ee Collider**		**LHC**	**HL-LHC**	
Plane	x	y	x	y	x y	x y	
Emittance [pm]	260	0.53	710	1.9	503	335	β [m]
Beam size σ [μm]	88.3	4.0	145.9	7.5	122.8	100.2	30
	114.0	5.2	188.4	9.7	158.6	129.4	50
	134.9	6.1	222.9	11.5	187.6	153.1	70
	153.0	6.9	252.8	13.1	212.8	173.6	90
	509.9	23.0	842.6	43.6	709.2	578.8	1000

The main goal of this table is to provide a comparative overview of the beam sizes in different scenarios. The beam size will scale with $\sqrt{\beta}$ for a given emittance. To obtain a clearer understanding of what the beam sizes will look like, Fig. 4.1.1 presents the

Gaussian distribution in one dimension (1D) and two dimensions (2D) for the FCC-ee Collider, LHC and HL-LHC beam sizes calculated for $\beta = 70\,\text{m}$ scaled to the number of particles in one bunch (see Table 4.1.1). Each plane has been plotted separately for the 1D distribution, Fig. 4.1.1a. In the 2D plot, Fig. 4.1.1b, the LHC beam is not included due to its similarity to the HL-LHC beam. The two distributions are shown with different density scales, as the maximum particle density varies by almost one order of magnitude.

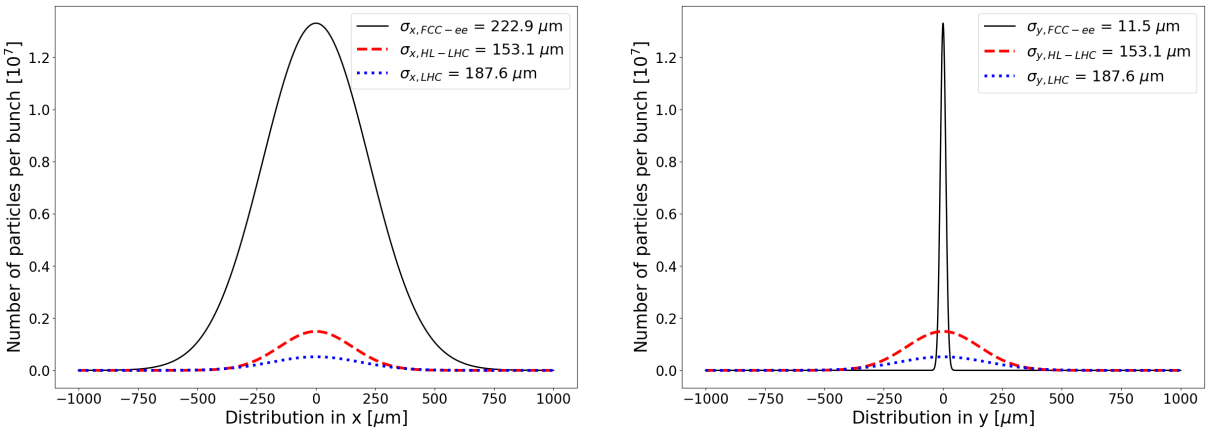

(a) One dimensional Gaussian distribution in the x and y plane.

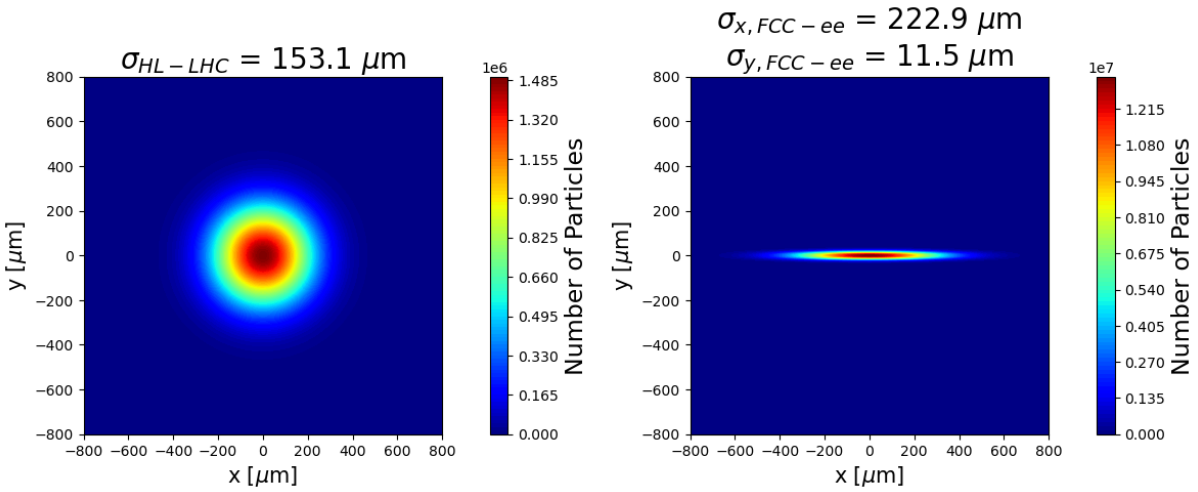

(b) Two dimensional Gaussian distribution.

Figure 4.1.1: Gaussian distribution in one (a) and two (b) dimensions for LHC, HL-LHC and FCC-ee Collider beam sizes calculated using $\beta = 70\,\text{m}$, scaled to the number of particles in one bunch (LHC: 1.15×10^{11} p^+, HL-LHC: 2.2×10^{11} p^+, FCC-ee: 2.14×10^{11} e^-/e^+).

Table 4.1.1 shows that the HL-LHC and FCC-ee beams have similar bunch intensities. The 2D distributions in Fig. 4.1.1b illustrate how the particles are spread out in these bunches. While the spread is comparable in the x-plane, the distribution is considerably more peaked in the y-plane, which leads to a significant difference in the maximum particle

density. The FCC-ee maximum particle density is about 10 times larger than the HL-LHC. This difference in magnitude is even more clearly shown in Fig. 4.1.1a, where the scaling for the number density is identical for all three beams.

While the spatial distributions of the beams provide valuable insights into their particle distributions, this alone does not fully characterize the beams' impact. The next section combines the spatial properties with the beam energy to estimate the energy density of the beams.

4.1.3 Average Energy Density Estimations

By approximating the area of the beam to be the product of the beam size σ in x and y, the energy density is given by Eq. 4.4.

$$\text{Energy density} = \frac{\text{Total Beam Energy}}{\text{Area}} = \frac{\text{Number of Particles} \cdot \text{Particle Energy}}{\sqrt{e_x \cdot e_y} \cdot \beta} \tag{4.4}$$

Since the particle distribution follows a Gaussian distribution, the product of the beam size in x and y will result in a rectangle in which a large proportion of the particles will pass through. Since σ is the rms value of the distribution, 68.27% [38] of the particles will pass through the area. Hence, when calculating the energy density of one bunch, the number of particles will be the bunch intensity of the beam, presented in Table 4.1.1, multiplied by 0.6827.

Table 4.1.4 presents the calculated beam energy density for three intensities of the FCC-ee Booster beam, the FCC-ee Collider beam, and the LHC and HL-LHC beams. The three chosen intensities for the FCC-ee Booster beam correspond to fractions of the total FCC-ee Collider beam intensity, specifically 0.5%, 1%, and 10%.

The results presented in Table 4.1.4 show that both the LHC and HL-LHC beams have significantly higher energy densities than the FCC-ee Booster and Collider beams when scaled to their bunch intensity. Closer comparisons of the HL-LHC and FCC-ee Collider beams explain why this is unsurprising. These beams have approximately the same amount of particles in their beam area, while the beam area of the FCC-ee beam is approximately 10 times smaller. However, the particle energy of the HL-LHC is about 150 times that of the FCC-ee. This results in a scaling of about 17 going from the energy density of the FCC-ee Collider beam to the HL-LHC beam. Doing the same for the LHC beams shows that the scaling for the FCC-ee Collider beam is approximately a factor 6.

A weakness of this method of calculating the energy density is that it assumes that the particles are distributed uniformly within the area and not Gaussian. However, since the cutoff for each distribution is uniquely defined by the rms beam size, the normalized shape of the Gaussian distribution remains consistent across all beams. Thus, the simplification

Table 4.1.4: Energy Density of the FCC-ee Booster Beam for Three Different Intensities, the FCC-ee Collider Beam, and the LHC and HL-LHC Beams

	FCC-ee Booster			**FCC-ee Collider**	**LHC**	**HL-LHC**	
Particle Type	Electron/Positron				Proton		
Particle Energy [GeV]	45.6				7000		
Emittance ϵ_x [pm]	260			710	503	335	
Emittance ϵ_y [pm]	0.53			1.9	503	335	
Percentage of Intensity	0.5%	1.0%	10%	100%	100%	100%	
68% Intensity [10^{10}]	0.07	0.15	1.46	14.61	7.85	15.02	β [m]
Energy density [kJ/mm^2]	15.2	30.3	303.5	969.9	5834.4	16759.0	30
	9.1	18.2	182.1	581.9	3500.7	10055.4	50
	6.5	13.0	130.1	415.7	2500.5	7182.4	70
	5.1	10.1	101.2	323.3	1944.8	5586.3	90
	0.5	0.9	9.1	29.1	175.0	502.8	1000

of assuming a uniform distribution introduces the same systematic approximation in all cases, ensuring the validity of the comparisons.

Analytical estimations provide an efficient way for understanding and comparing beam properties, offering valuable insights into scaling and relative behaviors. However, detailed simulations are essential to capture the complexity of particle-matter interactions. The following section aims to do this.

4.2 Energy Distribution in the Material

This section uses FLUKA to simulate the energy deposited inside the target material, which is then scaled to the number of particles in one bunch. The simulation parameters and results are presented for the same beam sizes that were discussed in Section 4.1.2.

4.2.1 Simulation Parameters

Since the FCC-ee beams and the LHC and HL-LHC beams have very different characteristics, two different approaches are used to simulate them. Some parameters, such as material properties, are kept identical in order to get comparable results. However, the FCC-ee beams are simulated in three dimensions (x, y z), whilst for the LHC and HL-LHC beams azimuthal symmetry is assumed, and we can thus use a cylindrical coordinate system (r, z, ϕ). Both setups use a graphite cylinder as target. The material properties

and main beam parameters are given in Table 4.2.1.

Table 4.2.1: FLUKA Target Material Parameters and Main Beam Parameters

	FCC-ee	**LHC / HL-LHC**
Material	Graphite	
Material Density [g/cm^3]	2.28	
Particle Type	Electron/Positron	Proton
Particle Energy [GeV]	45.6	7000
Number of Primaries	200 000	50 000

As discussed in Section 3.1, the choice of the number of particles is a compromise for minimizing both the statistical error and the computational time. FLUKA typically requires fewer primary particles for proton beams compared to electron beams due to the fundamental differences in their interactions with matter. Protons deposit energy in a more focused and gradual manner. Their trajectories are less affected by scattering, resulting in relatively predictable paths compared to electrons. Electrons undergo more complex scattering, requiring a larger number of primaries to capture the statistical variability and ensure accurate results. However, the complex scattering is less time consuming than the hadronic interactions of the protons, and thus the computational time of the electron beam simulation is typically lower.

3D Target Setup for the FCC-ee Beams

The file used to set up the FCC-ee simulations was provided by Anton Lechner [39].

Since the FCC-ee beam sizes are quite small, the coordinate system has to be segmented accordingly. For these simulations, the target has been defined as a 3 m long cylinder with a radius of 3 cm. However, since the energy is expected to be deposited close to the beam impact point, only a smaller rectangular sub-area has been segmented. The target parameters are presented in Table 4.2.2.

The segmented range in x goes from -1 cm to 1 cm with a bin size of 79.9 µm, and the range in y goes from -0.05 cm to 0.05 cm with a bin size of 3.6 µm, accounting for the significantly smaller beam size in this plane. In the z-plane, the entire target length is segmented with a bin size of 1 cm.

2D Target Setup for the LHC and HL-LHC Beams

The file used to set up the simulations of the LHC and HL-LHC beams is based on the one created for a previously conducted LHC beam impact study [16–18, 22].

Table 4.2.2: Target Parameters For the FCC-ee Beams Simulations

Target Radius [cm]	3
Target Length [m]	3
Segmentation Range in x [cm]	[-1,1]
Bin Size in x [µm]	79.7
Segmentation Range in y [cm]	[-0.05,0.05]
Bin Size in y [µm]	3.6
Segmentation Range in z [cm]	[0,300]
Bin Size in z [cm]	1

Since the round beam simulation setup is 2D and thus less complex, the target segmentation is more straightforward than the one presented for the FCC-ee beams. The energy deposition from the impact of the LHC and HL-LHC beams is expected to reach further into the material longitudinally and radially. Thus, the entire target is segmented.

Table 4.2.3: Target Parameters For the LHC and HL-LHC Beams Simulations

Target Radius [mm]	50
Target Length [m]	10
Radial Bin Size [µm]	50
Longitudinal Bin Size [cm]	1

4.2.2 Simulation Results

Figure 4.2.1 presents the energy deposition in the zx, zy, and xy-plane of the target when impacted by the FCC-ee collider beam for a beta function of $\beta = 70\,\text{m}$. The plots were made using Flair [40]. Note that each of the axes (x, y, z) are scaled differently according to the most suitable scale in each case. The target is 3 m long (Table 4.2.2), however here, the z-axis is only plotted until 1 m as most of the energy is deposited close to the beam impact point. The y-axis is plotted from $-0.05\,\text{cm}$ to $+0.05\,\text{cm}$, and the x-axis is plotted from $-0.2\,\text{cm}$ to $+0.2\,\text{cm}$ in Fig. 4.2.1a, and from $-0.05\,\text{cm}$ to $+0.05\,\text{cm}$ in Fig. 4.2.1c. The additional zoom in Fig. 4.2.1c is chosen to keep the axes symmetric in order not to distort the shape of the cross-sectional beam profile.

The three plots in Fig. 4.2.1 provide a visualization of the energy deposition profile per bunch of the FCC-ee collider beam with $\beta = 70\,\text{m}$. Each plot is a cross-section of the beam profile, Fig. 4.2.1a at $y = [-1.78\,\text{µm}, 1.78\,\text{µm}]$, Fig. 4.2.1b at $x = [-38.8\,\text{µm}, 38.8\,\text{µm}]$, and Fig. 4.2.1c at $z = [0\,\text{cm}, 1\,\text{cm}]$.

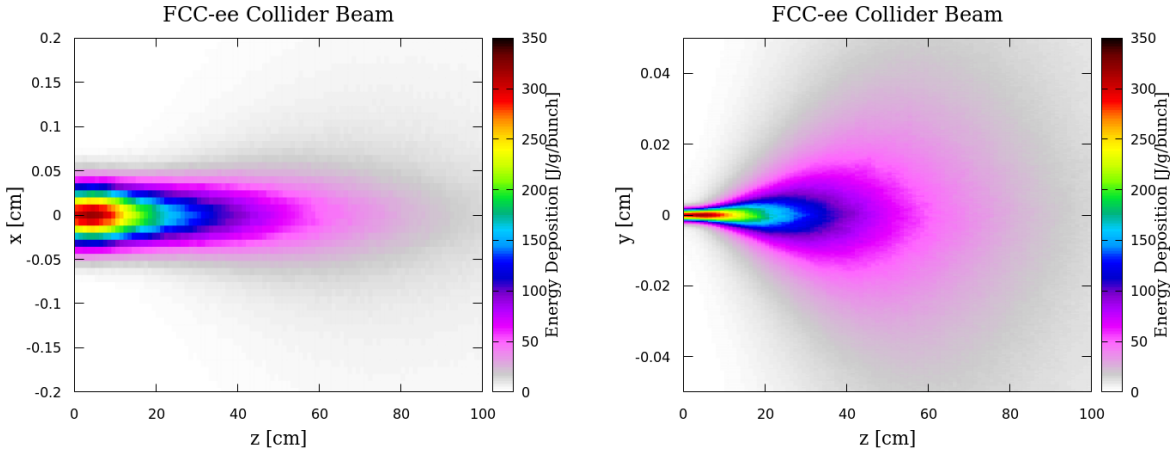

(a) zx-plane. **(b)** zy-plane.

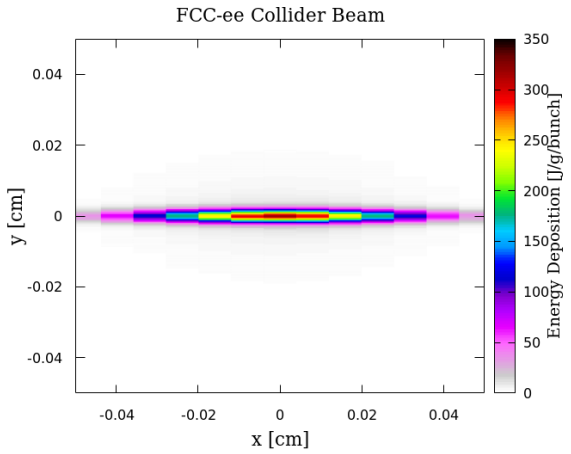

(c) xy-plane.

Figure 4.2.1: Energy deposition in the zx (a), zy (b), and xy-plane (c) of the target due to the impact of the FCC-ee Collider beam with $\beta = 70\,\mathrm{m}$.

The peak energy deposition is located longitudinally between $z = 3\,\mathrm{cm}$ and $z = 4\,\mathrm{cm}$ on the beam path (innermost bin of x and y). The precision of the location of the maximum is given by the chosen longitudinal binning of 1 cm.

Fig. 4.2.1a shows the energy deposition in the horizontal plane, while Fig. 4.2.1b shows it in the vertical plane. Both planes are symmetric around the beam path. In the horizontal plane, most of the energy is deposited within the first 500 µm, while vertically, a significant fraction is deposited within the first 50 µm. This difference is also illustrated in Fig. 4.2.1c.

The next step is to compare the simulation results for the different beam types and for different beam sizes. An important aspect is understanding how the maximum energy

deposition varies. To address this, Table 4.2.4 compares this value for the FCC-ee Booster beam at three intensities, the FCC-ee Collider beam, and the LHC and HL-LHC beams. All results are scaled to the intensity of one particle bunch.

Table 4.2.4: Maximum Energy Deposition Scaled to one Bunch Obtained From FLUKA Simulations of the FCC-ee Collider, FCC-ee Booster, LHC, and HL-LHC Beams Impacting on a Graphite Target With a Material Density of 2.28 g/cm^3

	FCC-ee Booster			**FCC-ee Collider**	**LHC**	**HL-LHC**	
Particle Type			Electron		Proton		
Particle Energy [GeV]			45.6		7000		
Emittance ϵ_x [pm]		260		710	503	335	
Emittance ϵ_y [pm]		0.53		1.9	503	335	
Percentage of Intensity	0.5%	1.0%	10%	100%	100%	100%	
Bunch Intensity [10^{11}]	0.01	0.02	0.21	2.14	1.15	2.20	β [m]
	10.0	20.0	200.0	688.7	337.7	701.0	30
Max. Energy	6.2	12.5	124.5	427.1	300.8	633.7	50
Deposition	4.6	9.2	92.0	317.5	277.9	574.4	70
[J/g/bunch]	3.6	7.2	72.0	249.0	263.3	557.9	90
	0.4	0.8	8.3	28.0	121.9	250.9	1000

The decrease of the maximum energy deposition for increasing β is more pronounced for the FCC-ee beams compared to the LHC and HL-LHC beams. Focusing on the FCC-ee Collider beam first, Table 4.2.4 shows that for $\beta = 30\,\text{m}$, the maximum energy deposition is 688.7 J/g/bunch. This is very similar to the corresponding HL-LHC value of 701.0 J/g/bunch and more than twice as high as the corresponding LHC value of 337.7 J/g/bunch. When β is increased to 50 m, the maximum energy deposition of the FCC-ee Collider beam is 427.7 J/g/bunch, which is in between the LHC and HL-LHC values of 300.8 J/g/bunch and 633.7 J/g/bunch. As β increases, the FCC-ee beam diverges from the HL-LHC values and becomes more similar to the LHC values. At $\beta = 90\,\text{m}$, the FCC-ee Collider and LHC results are very close, at 249.0 J/g/bunch and 263.3 J/g/bunch, however the HL-LHC result is now more than twice as high at 557.9 J/g/bunch. For $\beta = 1000\,\text{m}$, the maximum energy deposition of the FCC-ee beams is significantly lower than those of the LHC and HL-LHC beams.

The FCC-ee Booster beam shows the same trend as the FCC-ee Collider beam. In fact, for each increase in β, the maximum energy deposition of the FCC-ee Collider and Booster beams decreases with the same percentage, 38%, 26%, 22%, and 11%.

4.3 Analysis

4.3.1 Shape of Energy Deposition Shower

Table 4.2.4 shows the maximum energy deposition for all beams, however as seen in Fig. 4.2.1, it is equally important to understand how the energy deposition is distributed inside the target material. As discussed in Section 2.3, electron and proton beams behave differently when interacting with the material. To illustrate this, Fig. 4.3.1 compares the energy deposition in the zy-plane of the FCC-ee Collider beam with the zr-plane of the HL-LHC beam, both with $\beta = 30\,\text{m}$. These two beams are chosen because they have a similar maximum energy deposition. To emphasize the difference in how the energy is deposited throughout the material in the two cases, the scaling of the axes is kept identical.

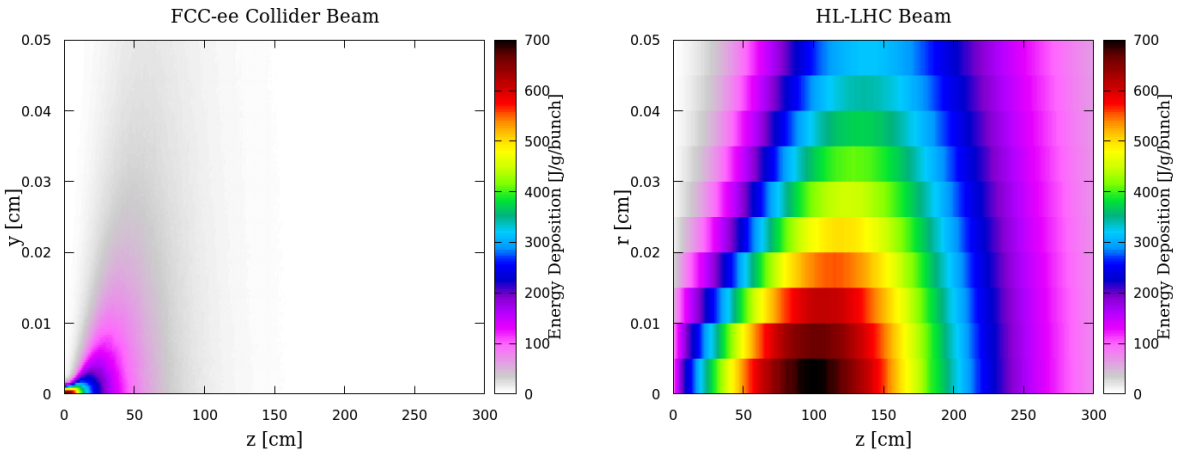

(a) FCC-ee collider beam.

(b) HL-LHC beam.

Figure 4.3.1: Comparison of the energy deposition in the zy-plane of the impact of the FCC-ee Collider beam, and the zr-plane of the HL-LHC beam. Both impacting beams have the same β function of $\beta = 30\,\text{m}$.

Figure 4.3.1a shows how the FCC-ee Collider beam deposits its energy close to the beam impact point. All energy is essentially deposited within the first 50 cm longitudinally and 0.01 cm horizontally. In contrast, Fig. 4.3.1b shows how the high-energy LHC proton beam deposits the energy deeper into the material. The peak of the energy deposition is located 110 cm inside the material. The radial reach is also significantly larger than the equivalent vertical reach for the FCC-ee Collider beam.

Figure 4.3.2 presents the same data as Fig. 4.3.1, but the scaling of the axes is adapted based on what represents the shape of each distribution the best. For the FCC-ee collider

beam, z is plotted to 100 cm and y to 0.05 cm, and for the HL-LHC beam z is plotted to 300 cm, and r to 0.5 cm.

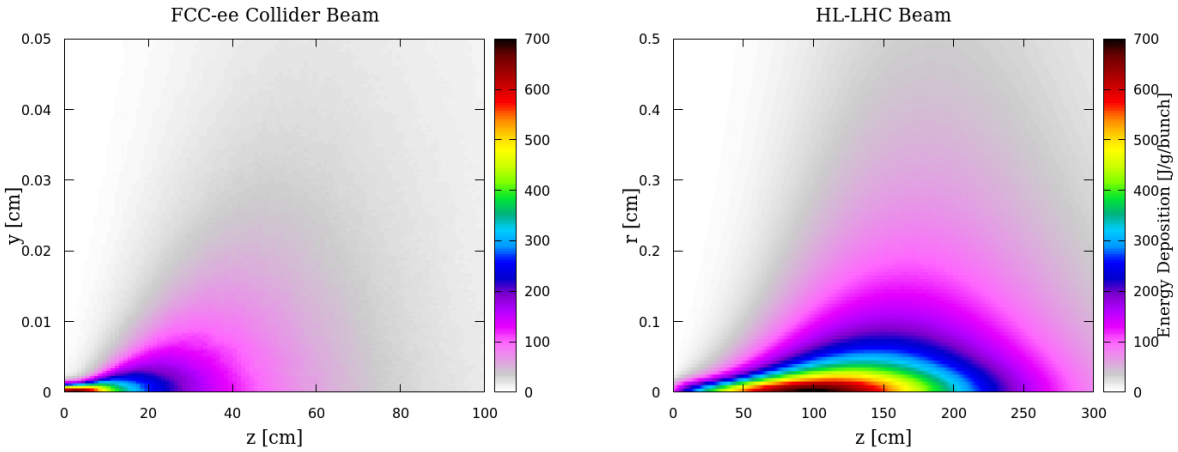

(a) FCC-ee Collider beam.

(b) HL-LHC beam.

Figure 4.3.2: Comparing the shape of the energy deposition in the zy-plane of the impact of the FCC-ee Collider beam and the zr-plane of the HL-LHC beam. Both impacting beams have the same β function of $\beta = 30$ m.

The shapes observed in Fig. 4.3.2 can be explained by how electrons/positrons, protons and their subsequent particle showers interact differently with the material. The HL-LHC beam (Fig. 4.3.2b), consisting of protons, deposits most of its energy further downstream in the material. The gradual increase from the impact point to this maximum is because the impacting protons first undergo hadronic interactions, producing secondary particles that transport the energy further into the material.

In contrast, the energy deposition maximum is located much closer to the target surface for the FCC-ee beams (Fig. 4.3.2a), consisting of electrons/positrons. This is because an electron directly undergoes electromagnetic processes, such as ionization of atoms and scattering. These processes will, in turn, produce electromagnetic showers that will build up much faster than the hadronic showers.

4.3.2 Maximum Energy Deposition For Various β-functions

Section 4.2.2 presented how the maximum energy deposition of the FCC-ee beams decreased faster as β increased than the maximum energy deposition of the LHC and HL-LHC beams. This section aims to explore and understand why this happens.

As discussed in Section 4.3.1, the energy deposition showers of electron/positron and proton beams develop differently. A proposed explanation for the observed trend in the maximum energy deposition is that the more peaked energy deposition shape of the

FCC-ee beams makes them more sensitive to changes in the beam size. To illustrate this, Fig. 4.3.3 shows the energy deposition after the impact of the FCC-ee Collider and HL-LHC beams along the beam path (Fig. 4.3.3a and 4.3.3c), and along a horizontal and radial line at the longitudinal position of the maximum energy deposition (Fig. 4.3.3b and 4.3.3d). The two latter figures include dotted lines representing the calculated beam sizes (Table 4.1.3) corresponding to the β-functions. For the FCC-ee collider beam, these values refer to the vertical beam size σ_y.

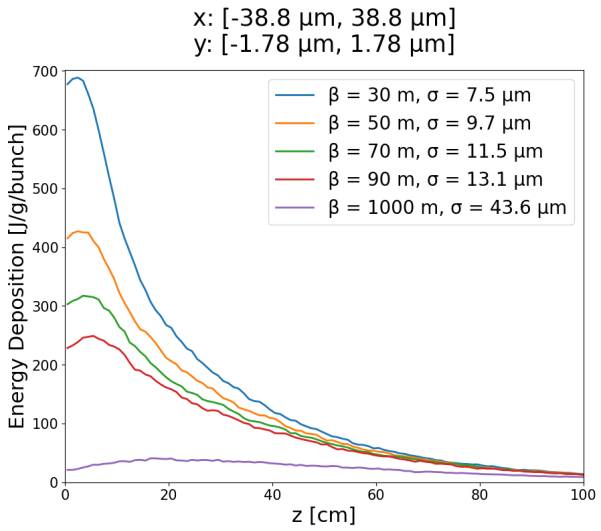

(a) z-axis, FCC-ee collider beam.

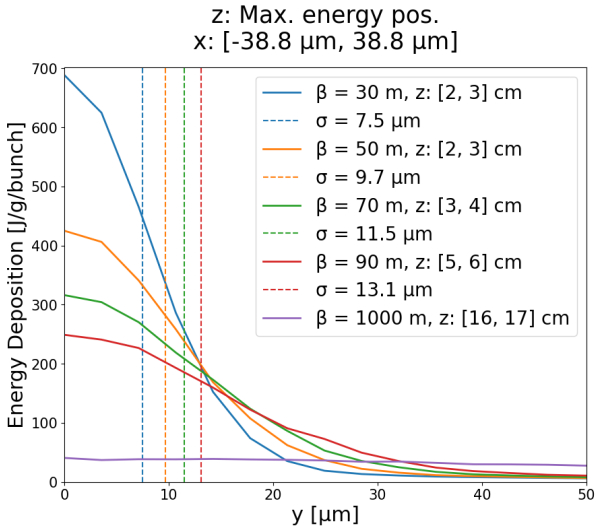

(b) y-axis, FCC-ee Collider beam.

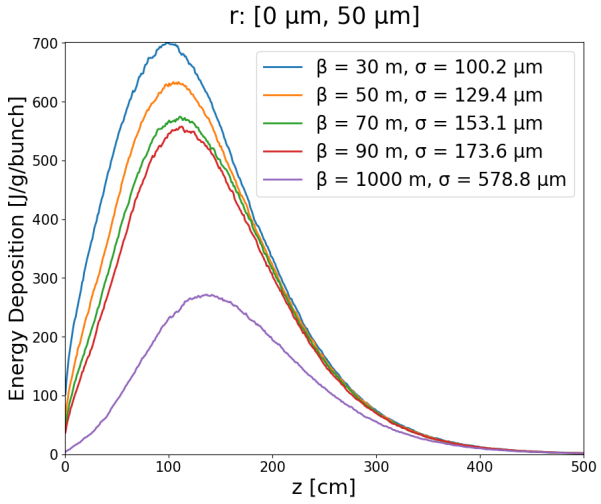

(c) z-axis, HL-LHC beam.

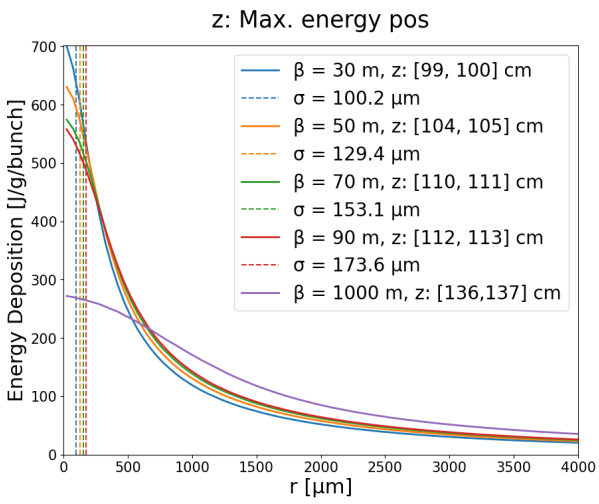

(d) r-axis, HL-LHC beam.

Figure 4.3.3: Energy deposition along the beam path z (a,c), along a vertical line y at the innermost x bin and the z bin of the maximum energy deposition the FCC-ee Collider beam (b), and along a radial line r at the z bin of the maximum energy deposition for the HL-LHC beams.

Each plot in Fig. 4.3.3a shows the energy deposition building up to its maximum value

and then decreasing towards zero further into the material. Longitudinally, Fig. 4.3.3a and 4.3.3c show that the maximum energy deposition of the FCC-ee Collider beam is consistently located significantly closer to the beam impact point than the maximum of the HL-LHC beam. The position of the maximum also moves less into the material. The difference between the location of the maximum in absolute value when $\beta = 30\,\text{m}$ and $\beta = 90\,\text{m}$ is only 3 cm, while the same difference for the HL-LHC beam is 13 cm.

For the evolution along the vertical line for the FCC-ee beam and the radial line for the HL-LHC beam, both Fig. 4.3.3b and 4.3.3d show that the maximum energy deposition is located along the beam path. Again, the energy deposition of the FCC-ee beam decreases significantly faster over the radial/vertical position. At around $y = 20\,\mu\text{m}$, almost no energy is deposited. This can be compared to $r = 2000\,\mu\text{m}$ for the HL-LHC beam.

This difference becomes even more evident when horizontal lines representing the corresponding beam sizes are included. For the FCC-ee collider beam, a large fraction of the energy is deposited within one beam sigma, while this fraction is significantly smaller for the HL-LHC beam. Hence, Fig. 4.3.3b and 4.3.3d show how the FCC-ee beam is much more sensitive to changes in the beam size.

4.3.3 Comparison with Representative LHC Beam Sizes

The previous sections have compared the FCC-ee, LHC, and HL-LHC beams, assuming the same β-functions. This section presents the calculated energy deposition for additional beam sizes relevant to beam operation in the LHC ring. Nominally, the maximum β-function in the arc for the LHC beam is 180 m [10, p.6], which corresponds to a beam size of 300 µm. However, in the context of machine protection studies, it is also relevant to study larger beam sizes. This is because, in scenarios where beam losses are more likely to happen, such as during injection or extraction or in the collimation system, the beam size is typically increased. For this reason, I have chosen to consider the following beam sizes in this section: 0.25 mm, 0.5 mm, 0.75 mm and 1.0 mm.

Table 4.3.1 presents the maximum energy deposition obtained from FLUKA simulations for the aforementioned beam sizes, scaled to LHC and HL-LHC intensities.

Comparing with the values in Table 4.2.4, it can be seen that for $\sigma = 0.25\,\text{mm}$, the maximum energy deposition for one bunch of the LHC beam is similar to the FCC-ee booster beam with 10% of the total beam intensity with $\beta = 30\,\text{m}$ (200.0 J/g/bunch) and the FCC-ee collider beam with $\beta = 90\,\text{m}$ (249.0 J/g/bunch). The HL-LHC beam has a maximum similar to the FCC-ee collider beam with $\beta = 50\,\text{m}$ (427.1 J/g/bunch).

In general, it can be concluded that the maximum energy deposition values obtained for the FCC-ee collider using arc β-functions are higher than those obtained for the LHC beam sizes with larger β-functions. The values for the FCC-ee booster with 10% of the

Table 4.3.1: Maximum Energy Deposition Obtained from FLUKA Simulations Using Four Beam Sizes that are Relevant for Beam Operation in the LHC ring, Scaled to LHC and HL-LHC Bunch Intensities

	Maximum Energy Deposition [J/g/bunch]	
σ [mm]	**LHC**	**HL-LHC**
0.25	235.1	449.8
0.5	153.9	294.4
0.75	115.7	221.4
1.0	92.4	176.7

beam intensity are more comparable. For the HL-LHC beam, the three smaller beam sizes result in maximum energy deposition values that are in the same range as the ones found for the FCC-ee Collider beam (249.0 J/g/bunch to 688.7 J/g/bunch).

The beam sizes 0.5 mm and 1.0 mm are especially interesting to discuss as these have previously been used to conduct full beam impact studies [17, 18, 20], i.e. simulation of a large number of bunches. These studies have found that, due to hydrodynamic tunneling, the energy deposition will reach longitudinally further into the material than expected from static simulations. From a machine protection perspective, this longitudinal tunneling range is interesting, and conducting a full study of the FCC-ee beams is crucial to gain an understanding of their damage potential. A key question is thus whether hydrodynamic tunneling will also occur for the impact of the FCC-ee beams. Because the initial impact of the FCC-ee beams results in maximum energy depositions in similar ranges as the LHC and HL-LHC beams, the current hypothesis is that hydrodynamic tunneling will occur. However, a full beam impact study is necessary to confirm this. The first steps for this study are presented and discussed in the following chapter.

Chapter 5

INITIAL IMPACT OF THE ROUND FCC-ee BEAM

This chapter presents the results of the initial beam impact simulations of the FCC-ee beam. Here, the impact of the first five bunches is simulated using Autodyn. In these simulations, the FCC-ee beam is approximated as a round beam. This approximation is justified as a reasonable starting point for FCC-ee beam impact studied as it emphasizes the maximum energy deposition in the center, and results from previous beam impact studies [17, 20] suggest that this value is of high importance for the total reached damage range of the full beam impact. Furthermore, a round beam allows for a 2D simulation setup due to azimuthal symmetry, which greatly reduces the complexity and the computational costs of the study.

The simulations are carried out using one initial FLUKA simulation of the initial target material, and then ANSYS Autodyn simulates the material's hydrodynamic response. The aim is to gain insight into how the density depletes, the temperature increases, and the pressure evolves during the initial impact of the FCC-ee beam. The results are then compared to the impact of the LHC and HL-LHC beams.

5.1 Round Beam Approximation

The first step is to develop a round beam approximation for the initially asymmetric and flat FCC-ee beam. The flat FCC-ee Collider beam corresponding to $\beta = 70\,\mathrm{m}$, so $\sigma_x = 222.9\,\mu\mathrm{m}$ and $\sigma_y = 11.5\,\mu\mathrm{m}$, is used as a reference beam. The Collider beam is chosen over the Booster beam because of the higher beam intensity, and $\beta = 70\,\mathrm{m}$ is chosen as a midpoint in the range of arc β-function values.

Two approaches for approximating the flat beam to a round one are presented. The first one starts by estimating the beam area as the product of the beam size in the x- and y-plane and then finds a round beam size that results in the same area as the reference flat beam. The second approach uses the beam size in the y-plane and adjusts the particle density to the value reached in the center of the flat FCC-ee beam. In the following sections, both approaches are explained in depth and explored analytically and through FLUKA simulations in order to decide which is more suitable.

5.1.1 Methods for Approximating the Round Beam

Method 1: Equating the Area of the Flat and Round Beam

By selecting a round beam with an equivalent area to the flat beam, the total beam intensity and the number of electrons are conserved. As previously noted, the Gaussian distribution of particles within the beam allows for a simplified estimation of the beam area, which can be approximated as the product of the beam sizes in the x- and y-planes. Consequently, the beam size of a round beam with an equivalent area to the flat beam can be determined using Eq. 5.1.

$$\sigma_1 = \sqrt{\beta \cdot \sqrt{e_x \cdot e_y}} \tag{5.1}$$

Using $\beta = 70\,\text{m}$ and the FCC-ee Collider emittances, we obtain $\sigma_1 = 50.5\,\mu\text{m}$, where the subscript 1 represents method 1.

Method 2: Circular Cutoff From the Center of the Flat Beam

As mentioned in the introduction to this chapter, previous beam impact studies have suggested that the energy deposition along the beam axis is important in estimating the damage range of a full beam impact. This is where the maximum energy deposition is found, and the value rapidly decreases outwards in the material. Therefore, the idea of the second method is that an efficient way of approximating the flat FCC-ee beam is to use a circular cutoff from the center of the beam, assuming that this circular cutoff will give similar results on the beam axis as the flat beam. For the FCC-ee collider beam with $\beta = 70\,\text{m}$ this implies using a beam size of $\sigma_2 = 11.5\,\mu\text{m}$ in both planes, where the subscript 2 represents method 2.

If a small part of the FCC-ee beam is cut out, the electron density has to be adjusted accordingly. The electron density N is found by relating the number of electrons n_e to the area in which the electrons are impacting, see Eq. 5.2. For the purposes of this section, n_e is the bunch intensity.

$$N \propto \frac{n_e}{\sigma_x \cdot \sigma_y} \tag{5.2}$$

Requiring that the electron density of the approximated round beam has to be equal to the electron density of the round beam ($N_{round} = N_{flat}$), and using that $\sigma = \sqrt{\beta\epsilon}$, we obtain the relation presented in Eq. 5.3.

$$n_{e,\text{round}} = \frac{n_{e,\text{flat}}}{\beta\sqrt{e_x \cdot e_y}} \cdot \beta e_y = n_{e,\text{flat}} \cdot \sqrt{\frac{e_y}{e_x}} = n_{e,\text{flat}} \cdot 0.05173 = 1.11 \times 10^{10} e^-/e^+ \tag{5.3}$$

To summarize, the proposed approximated round beam using method 2 has a beam size of $\sigma_2 = 11.5\,\mu\text{m}$ and an intensity of $1.11 \times 10^{10}\ e^-/e^+$ per bunch.

5.1.2 Gaussian Distributions of Approximated Round Beams

To decide which of the methods to use, the first step is to compare the particle distributions. Figure 5.1.1 shows the 2D Gaussian distribution of the two approximated round beams ($\sigma_1 = 50.7\,\mu\text{m}$ and $\sigma_2 = 11.5\,\mu\text{m}$), and compares it to the flat beam distribution. For better comparison, all distributions are shown on the same scale for the particle density. For a more detailed and quantitative comparison, Fig. 5.1.2 shows the 1D Gaussian distribution in x and y.

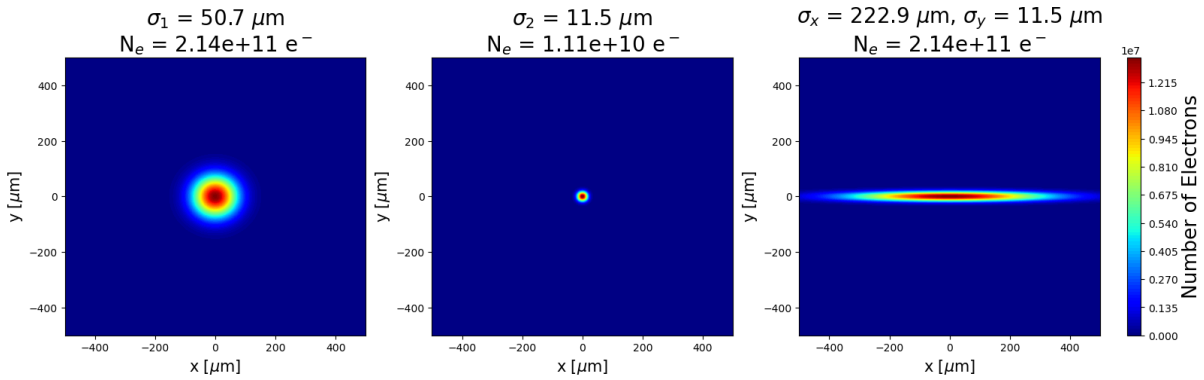

Figure 5.1.1: 2D Gaussian distribution for the two approximated round beams ($\sigma_1 = 50.7\,\mu\text{m}$ and $\sigma_2 = 11.5\,\mu\text{m}$) and the flat beam with $\sigma_x = 222.9\,\mu\text{m}$ and $\sigma_y = 11.5\,\mu\text{m}$.

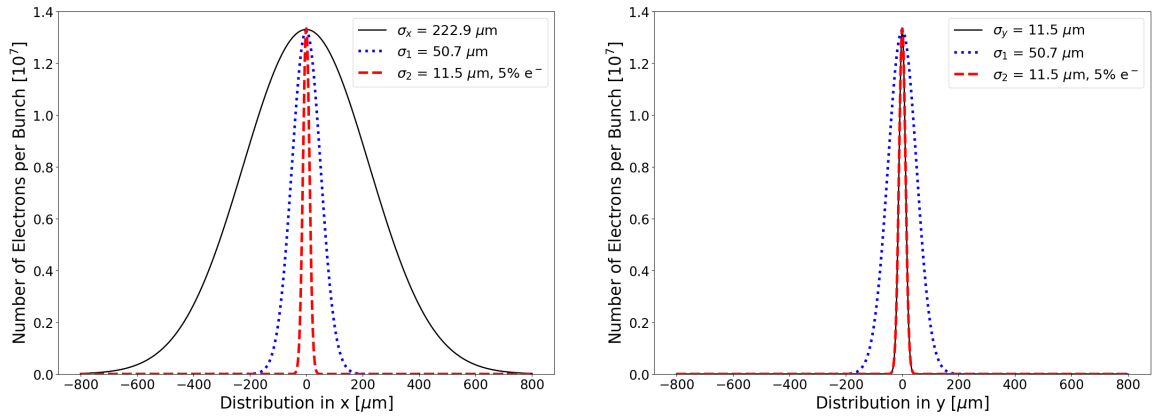

Figure 5.1.2: 1D Gaussian distribution of the electron density in x and y for the two approximated round beams ($\sigma_1 = 50.7\,\mu\text{m}$ and $\sigma_2 = 11.5\,\mu\text{m}$) and the flat beam with $\sigma_x = 222.9\,\mu\text{m}$ and $\sigma_y = 11.5\,\mu\text{m}$.

The first method maintains the beam area and the numbers of electrons/positrons, so it is essentially just a reshaping of the flat beam. The second round beam, σ_2, is

significantly smaller. The visualization highlights the key difference between the two methods. The first method maintains the total particle density, and the second maintains the vertical beam size while reaching the same central peak density.

Both methods accurately reproduce the maximum particle density at the center of the beam. However, both beams deviate significantly from the real distribution, as expected. To better understand how this discrepancy impacts the energy density distribution, FLUKA simulations are employed to determine which of the round beams more accurately represents the flat one.

5.1.3 Energy Deposition Comparison

The simulation parameters used are presented in Table 5.1.1. The simulation setup is similar to the one previously described for the 2D beams in Section 4.2.1.

Table 5.1.1: Parameters For Simulating the Approximated Round Beams

Beam Energy [GeV]	45.5
Particle Type	Electron
Target Radius [mm]	1
Number of Bins Radially	400
Target Length [m]	5
Number of Bins Longitudinally	1000
Number of Primaries	200 000

The simulated energy deposition of the two approximated round beams are presented in Fig. 5.1.3a and 5.1.3b. For comparison, the energy distribution in the xz- and yz-plane for the flat FCC-ee Collider beam is also included in Fig. 5.1.3c and 5.1.3d. Table 5.1.2 presents the maximum energy deposition values.

Table 5.1.2: Maximum Energy Density Obtained After First FLUKA Simulation for the two Round Beams Compared with the FCC-ee Collider Beam with $\beta = 70\,\mathrm{m}$

	σ [µm]	N_e	$\mathrm{E}_{\mathrm{max}}(\sigma)$ [J/g/bunch]	$\mathrm{E}_{\mathrm{flat}}$ [J/g/bunch]
Method 1	50.7	2.14×10^{11}	449.7	317.5
Method 2	11.5	1.11×10^{10}	304.4	

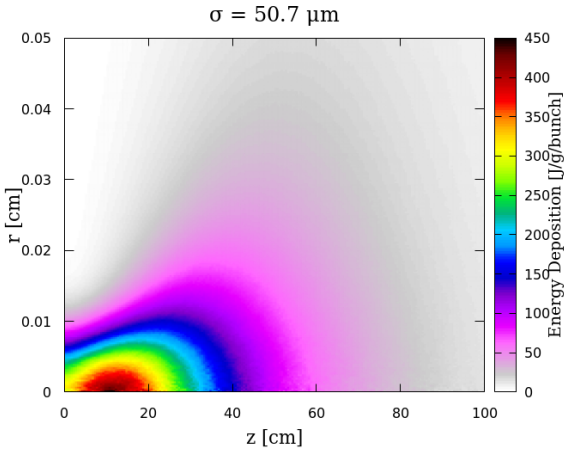

(a) Round beam with $\sigma_1 = 50.7\,\mu m$.

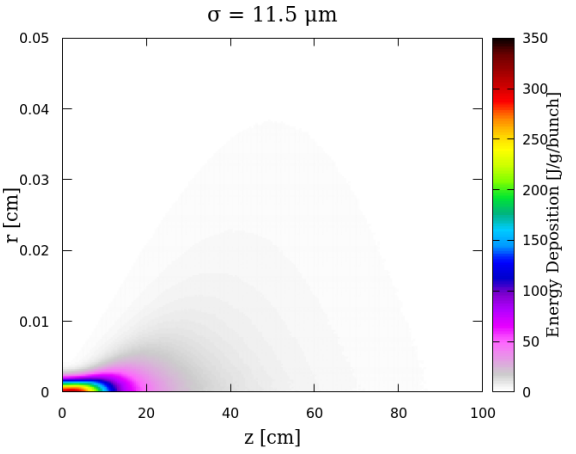

(b) Round beam with $\sigma_2 = 11.5\,\mu m$.

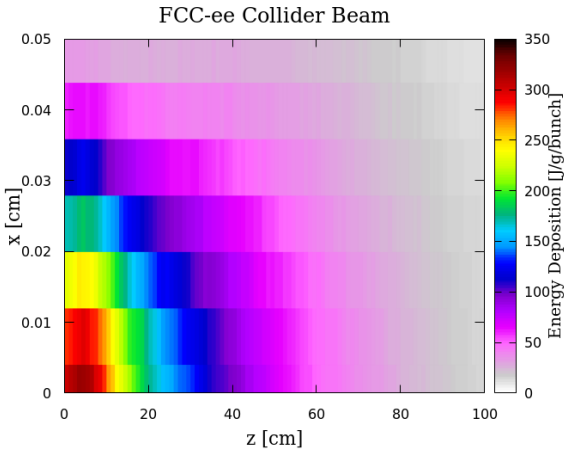

(c) zx-plane for the FCC-ee collider beam.

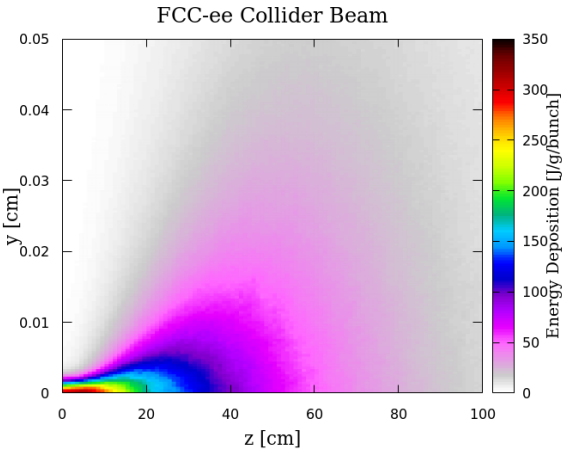

(d) zy-plane for the FCC-ee collider beam.

Figure 5.1.3: Comparison of the energy deposition of the impact of the two approximated round beams with the energy deposition in the zx- and zy-plane for the flat FCC-ee Collider beam.

The maximum energy deposition value using method 1, 449.7 J/g/bunch, is significantly higher than the reference value of the flat beam, 317.5 J/g/bunch. Looking at the shape of the distribution in Fig. 5.1.3a, it is not particularly comparable with either the zx- or zy-plane of the flat FCC-ee beam. In a way, this method attempts to take both of these planes into consideration. While the energy deposition shower at large z and r values more closely resembles the zy-plane of the flat FCC-ee beam compared to method 2 in this range, both the location and value of the peak energy deposition are quite off.

While the goal is to match the peak energy deposition with the reference peak, aligning the shape of the distribution can also be of interest. To achieve this, one proposed solution

is to increase the beam size to reduce the maximum energy deposition to match the reference value. This approach uses method 1 as a baseline and results in a beam profile that roughly aligns with the shape of the reference energy distribution and matches the peak value. The location of the maximum value will still remain inaccurate.

The result obtained from a sweep of beam sizes is presented in Table 5.1.3.

Table 5.1.3: Maximum Energy Deposition Obtained from Simulating a Range of Beam Sizes

σ_1	$E_{max}(\sigma)$ [J/g/bunch]
62	317.4
63	309.3
63	337.2

The results from Table 5.1.3 show how, if preferring an approximation that keeps the overall shape of the energy distribution while maintaining a maximum value similar to the reference beam, a round beam size of $\sigma_1 = 62.0\,\mu m$ should be used.

On the other hand, method 2 yields an initial result for the maximum energy deposition, 317.5 J/g/bunch, that is already very close to the reference value. Looking at the shape of the distribution in Fig. 5.1.3b, one can see that the range of the energy deposition is significantly lower. However, it reproduces the impact for the first 10 cm in the zy-plane quite accurately. This result is not surprising because this method is only based on this plane and not the zx-plane. The goal of the method is to simulate the maximum distribution along the beam path, and it does this for the most beam-heated region within the first 10 cm.

5.1.4 Conclusion for the Round Beam Approximation

Ultimately, the goal is to conduct a study that simulates the entire FCC-ee beam, not just the first five bunches. The aim of the study is to estimate how far into the material the damage will reach, and the most important contribution is given by the energy deposition along the beam axis, i.e. the z-axis.

Based on this, this section concludes that the round beam approximation using method 2 is the most promising. Simulated results further out in the material, both radially and longitudinally, will underestimate the energy deposited.

Since the justification is based on matching the reference maximum energy deposition, it is beneficial to adjust the parameters of the approximated beam so that they match perfectly. This can be done either by slightly adjusting the beam size or the bunch intensity. Because the found value of the bunch intensity used that the area of the beam

is the product of the beam size in x and y, and this itself is an approximation, it is concluded that adjusting this number is the best solution. The calculation is done below.

$$n_{e^-} = 1.11 \times 10^{10} e^-/e^+ \cdot \frac{\mathrm{E_{flat}}(\beta = 70\,\mathrm{m})}{\mathrm{E_{max}}(\sigma_2)} = 1.16 \times 10^{10} e^-/e^+ \tag{5.4}$$

The conclusion of this section is that the study will use a beam size $\sigma = 11.5\,\mu\mathrm{m}$ and a bunch intensity of $n_e = 1.16 \times 10^{10} e^-/e^+$.

5.2 Simulation Setup and Parameters

5.2.1 FLUKA Setup and Beam Parameters

Table 5.2.1 presents the FLUKA and beam parameters used in the simulations. The choice of value for the beam size and the number of electrons per bunch is discussed in Section 5.1.

Table 5.2.1: FLUKA and Beam Parameters

Particle Type	Electron
Beam energy [GeV]	45.6
Beam Size σ [µm]	11.5
Total Number of Bunches	11200
Electrons per Bunch	1.16×10^{10}
Bunch spacing [ns]	25

The target setup is similar to the 2D setup described in Section 4.2.1 but scaled down to accommodate the smaller beam size. The target parameters are presented in Table 5.2.2.

Table 5.2.2: FLUKA Target Parameters

Material	Graphite
Material Density [g/cm^3]	2.28
Target Radius [mm]	1.0
Target Length [m]	5
Radial Target Segmentation [µm]	2.5
Longitudinal Target Segmentation [mm]	5

The target is a cylinder with a length of 5 m and a radius of 1 mm. Radially, the bins have a size of 2.5 µm, and longitudinally of 5 mm.

5.2.2 Autodyn Setup and Parameters

Table 5.2.3 presents the main Autodyn simulation parameters used to simulate the round FCC-ee beam. For general simulation parameters see Section 3.2.

Table 5.2.3: Autodyn Simulation Parameters

Target Radius [mm]	1.0
Target Length [m]	5
Longitudinal Element Size [mm]	2
Radial Element Size (up to $r = 0.4\,\text{mm}$) [µm]	2.5
Electrons per Bunch	1.16×10^{10}
Time Step of One Cycle [ns]	0.125

The size of the target is the same as in the FLUKA simulations, however the segmentation is different. Longitudinally, a constant element size of 2 mm is kept along the entire target. Radially, the element size is 2.5 µm from $r = 0\,\text{mm}$ to $r = 0.4\,\text{mm}$. After this, a biased grid is implemented, meaning a grid with continuously increasing element size. The time step of 0.125 ns corresponds to one cycle in Autodyn. To simulate the impact of one bunch, 200 cycles are required, i.e. 25 ns.

5.3 Simulation Results

Figure 5.3.1a shows the result of the initial FLUKA simulation. Note that it is the same plot as in Fig. 5.1.3b, but scaled to $r = 0.02\,\text{cm}$. It shows how the energy is distributed in the initial material with a uniform density. Over time, the energy deposition will cause the density to deplete, as seen in Fig. 5.3.1b. The shape of the density depletion corresponds to the shape of the energy deposition, as it is the dynamic response of the material due to the energy being deposited. The minimum density value reached is $2.217\,\text{g/cm}^3$, which is a 2.27% decrease from the nominal density of graphite of $2.28\,\text{g/cm}^3$. The density is mainly depleted in the first 10 cm of the material, corresponding to the area where most of the energy is deposited.

The temperature, seen in Fig 5.3.1c, reaches a maximum value of 1332 K. The heating of the material is localized close to the impact point of the beam, and the shape throughout the material is similar to the energy deposition as these are related phenomena. The pressure, however, is not a localized phenomenon, as visible in Fig 5.3.1d. It oscillates between a maximum and minimum value radially, while the amplitude of the oscillations is continuously damped. Longitudinally, a front of low positive pressure is created.

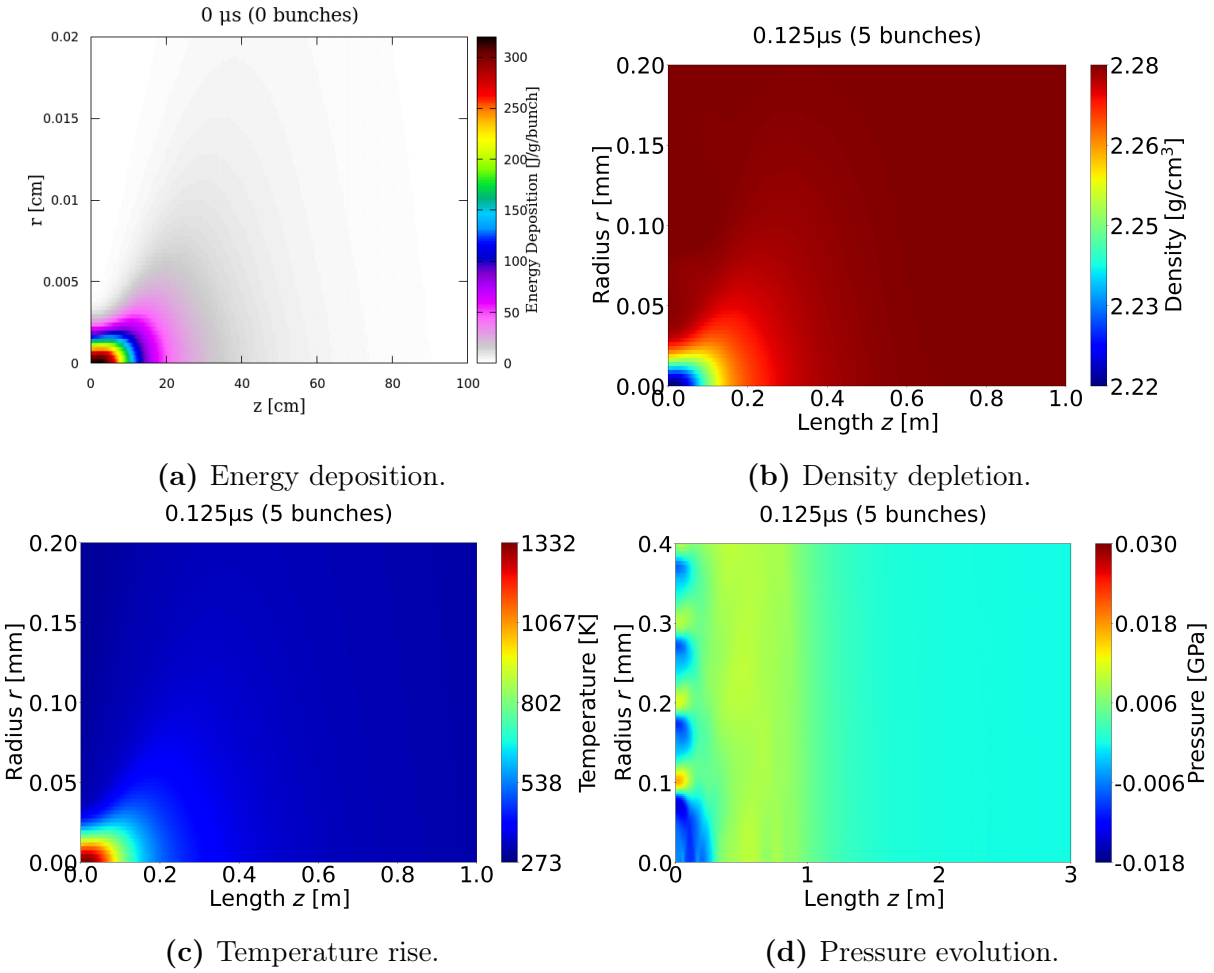

(a) Energy deposition.

(b) Density depletion.

(c) Temperature rise.

(d) Pressure evolution.

Figure 5.3.1: Energy distribution (a) of the material before impact simulated with FLUKA, and the density (b), temperature (c) and pressure (d) in the material after the impact of 5 bunches as simulated with Autodyn.

In Appendix A.1, A.2 and A.3, the distribution of density, temperature, and pressure, respectively, is plotted for each of the five impacting bunches.

5.4 Analysis

5.4.1 Comparison with LHC and HL-LHC Beam Impacts

In this section, data from previously conducted studies on the impact of the LHC beam [17, 18] and HL-LHC beam is analyzed and compared to FCC-ee results. These studies have analyzed the full beam impact, but for this analysis I will only consider the results from the impact of the first five bunches. The LHC and HL-LHC beams have been simulated using $\sigma = 0.5\,\text{mm}$, considerably larger than the beam size used for the FCC-ee study.

Table 5.4.1 presents the maximum energy deposition obtained by the FLUKA simulations for the round FCC-ee beam (45.6 GeV, $\sigma = 11.5\,\mu m$, 1.16×10^{10} e^+/e^-), the LHC beam (7000 GeV, $\sigma = 0.5\,mm$, 1.15×10^{11} p^+) [17, 18], and the HL-LHC beam (7000 GeV, $\sigma = 0.5\,mm$, 2.2×10^{11} p^+). All values are scaled to the number of particles in one bunch.

Table 5.4.1: Maximum Initial Energy Deposition Scaled to One Bunch

	FCC-ee	**LHC**	**HL-LHC**
Maximum Initial Energy Deposition [J/g/bunch]	317.5	153.9	294.4

Table 5.4.2: Comparison of the maximum temperature and pressure, the minimum density, and the percentage decrease from the initial nominal graphite density ($2.28\,g/cm^3$) for the approximated round FCC-ee beam (45.6 GeV, $\sigma = 11.5\,\mu m$, 1.16×10^{10} e^+/e^-), the LHC beam (7000 GeV, $\sigma = 0.5\,mm$, 1.15×10^{11} p^+) [17, 18], and the HL-LHC beam (7000 GeV, $\sigma = 0.5\,mm$, 2.2×10^{11} p^+) for the impact of the first five bunches

	Number of Bunches	**1**	**2**	**3**	**4**	**5**
FCC-ee	Max. Temperature [K]	600	810	993	1166	1332
	Max. Pressure [GPa]	0.029	0.020	0.018	0.017	0.017
	Min. Density [g/cm^3]	2.265	2.252	2.240	2.228	2.217
	% Decrease in Density	0.67	1.22	1.75	2.26	2.77
LHC	Max. Temperature [K]	470	595	700	800	892
	Max. Pressure [GPa]	0.13	0.23	0.31	0.38	0.44
	Min. Density [g/cm^3]	2.280	2.280	2.279	2.278	2.276
	% Decrease in Density	0	0	0.04	0.09	0.18
HL-LHC	Max. Temperature [K]	585	783	956	1122	1279
	Max. Pressure [GPa]	0.22	0.39	0.53	0.65	0.76
	Min. Density [g/cm^3]	2.280	2.280	2.278	2.276	2.273
	% Decrease in Density	0	0	0.09	0.18	0.31

The HL-LHC beam has an initial maximum energy deposition of 294.4 J/g/bunch, similar to the value of 317.5 J/g/bunch for the round FCC-ee beam. On the other hand, the LHC beam has a maximum value of 153.9 J/g/bunch, corresponding to the lower bunch intensity.

Table 5.4.2 shows the maximum temperature and pressure, the minimum density, and the percentage decrease from the initial nominal graphite density of 2.28 g/cm^3 for the three studies.

The temperature reaches similar maximum values for the round FCC-ee beam and the HL-LHC beam after the impact of each bunch. The minimum material density in the target decreases significantly faster for the round FCC-ee than for both the LHC and HL-LHC beams. After five bunches, the density is depleted by 2.77%.

To understand this difference, Fig. 5.4.1 compares the energy deposition for the round FCC-ee and the HL-LHC beam. The results of the LHC beam for this initial simulation are the same as for the HL-LHC beam, just scaled to a different bunch intensity, and are therefore not included here.

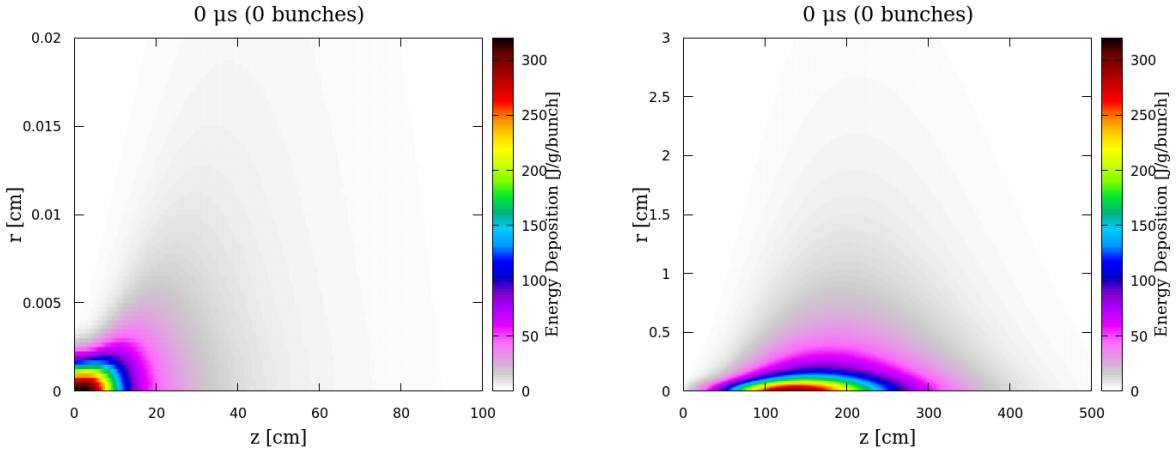

(a) FCC-ee. **(b)** HL-LHC.

Figure 5.4.1: Comparing the energy deposition obtained after the first FLUKA simulation of the approximated round FCC-ee beam and the HL-LHC beam. The scaling of the axis is defined after what is suitable in each case.

The energy deposition for the FCC-ee beam is significantly more localized than the energy deposition for the HL-LHC beam, especially in the radial direction. The energy is also deposited closer to the beam impact point. For the round FCC-ee beam, the peak is located at around 2 cm, whilst for the HL-LHC beam, it is located around 1.4 m. The reason for this is already discussed in Section 4.3.1.

The difference in the energy deposition shower for the two beams also affects how the

hydrodynamic parameters evolve throughout the material. Figure 5.4.2 compares the 2D density distribution in the material after the impact of five bunches of the FCC-ee beam and the HL-LHC beam.

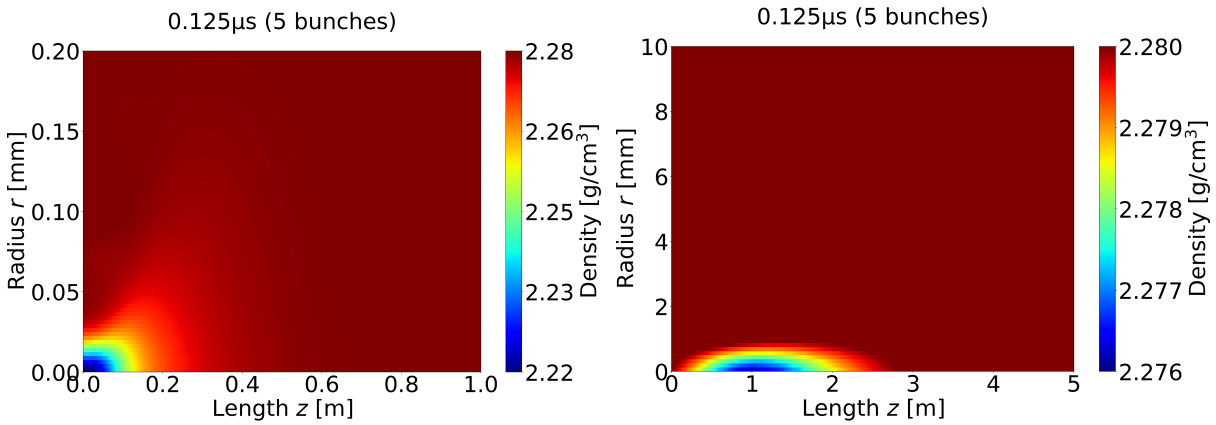

(a) FCC-ee. **(b)** LHC.

Figure 5.4.2: Comparing the density distribution after the impact of 5 bunches for the FCC-ee beam (a) and the LHC beam (b).

Figure 5.4.2 shows that the shape of the density depletion directly results from the shape of the energy deposition. Note that in Fig. 5.4.2a, the minimum density is 2.22 g/cm^3, while in Fig. 5.4.2b it is 2.276 g/cm^3.

Figure 5.4.3 depicts the evolution of density and temperature along the beam axis over the five simulation time steps.

Comparing the time evolution of the density depletion for the round FCC-ee beam (Fig. 5.4.3a) and the HL-LHC beam (Fig. 5.4.3c) along the beam axis shows that the density is depleted much faster for the round FCC-ee beam and that the depletion occurs significantly closer to the beam impact point. For the HL-LHC beam, the density is depleted mostly between 1 m and 2 m, while for the round FCC-ee beam, the depletion is limited to the first 0.5 m. The temperature rise also happens in these same longitudinal ranges, while both the round FCC-ee beam and HL-LHC beam reach the same maximum temperature values.

Note that the chosen target segmentation for the FCC-ee study (2.5 µm) and the LHC and HL-LHC studies (125 µm) are quite different. This means that FLUKA averages the energy deposition over areas of 0.001 25 mm^2 and 3.125 mm^2, respectively. While this is important to keep in mind for comparison, it does not impact the actual values presented.

Another interesting point is how the hydrodynamic parameters will continue to evolve over time. Looking at the evolution of density and temperature in Fig. 5.4.3c and 5.4.3d, already after only the impact of 5 bunches, the hydrodynamic change has reached quite far into the material. Results from the full beam impact studies have found that the

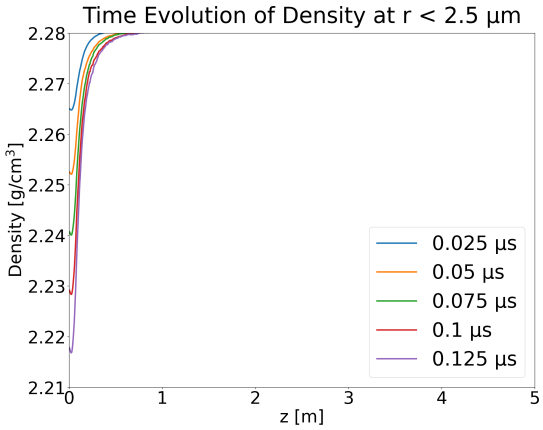

(a) FCC-ee.

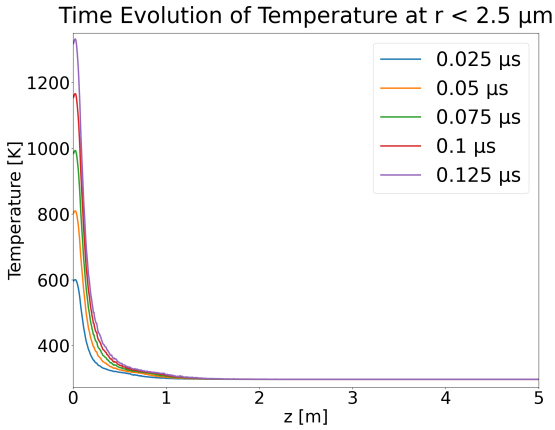

(b) FCC-ee.

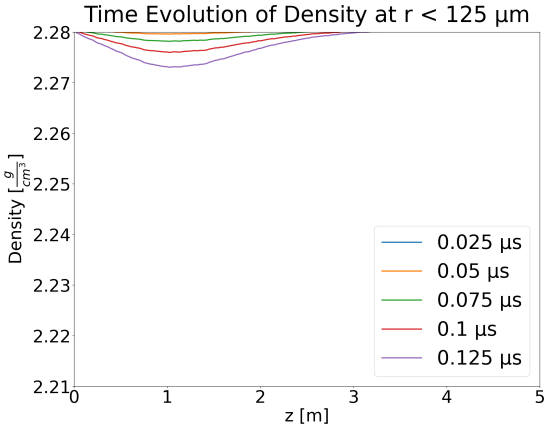

(c) HL-LHC.

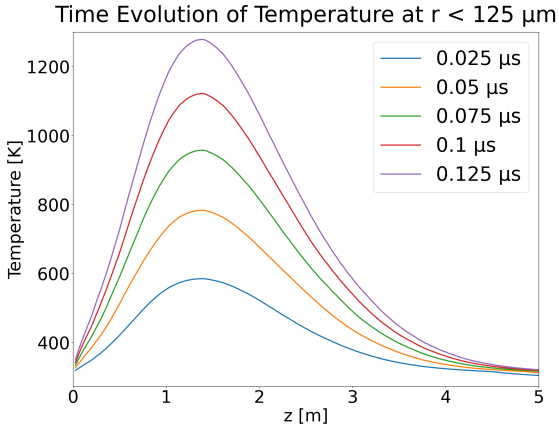

(d) HL-LHC.

Figure 5.4.3: Time evolution of the density depletion and temperature rise on the beam axis for the approximated round FCC-ee beam and the HL-LHC beam.

impact of the full LHC beam will reach around 20 m into the material [17, 18], and the HL-LHC will reach about 30 m into the material [20]. A full study is needed to estimate the tunneling range of the round FCC-ee beam. However, after the impact of the first five bunches, there is significant less longitudinal reach. The FCC-ee beam consists of 11 200 bunches, compared to the nominal values of 2808 for the LHC beam and 2760 for the HL-LHC beam, so it would be very interesting to see how this would evolve over time.

This section still has not addressed an important part of Table 5.4.2, namely the evolution of the pressure. Here, the round FCC-ee beam causes significantly lower peak pressure values than both the LHC and HL-LHC beams. Additionally, as seen in Section 5.3, the pressure of the FCC-ee beam oscillates radially between a maximum and a minimum value, a behavior not observed for the LHC and HL-LHC beams. This difference will be explored in greater detail in the next section.

5.4.2 Time Evolution of Pressure

Figure 5.3.1d poses quite a few discussion points when it comes to the pressure. It spreads radially much more significantly than the energy, density, and temperature, oscillating between a minimum and maximum value that gradually attenuates. When plotting the pressure at each simulation time step (Fig. A.3.1 in A.3), it is seen that the impact of each bunch results in an oscillation. Figure 5.4.4 shows this for the impact of the three first bunches. In addition, the radial evolution at $z = 2\,\text{cm}$ is presented next to its corresponding 2D plot to emphasize the oscillating wave.

The initial peak pressure of 0.029 GPa is reached after the impact of the first bunch, along with the minimum value of $-0.018\,\text{GPa}$. Over time, both of these values attenuate, the maximum more than the minimum. The impact of each new bunch results in a new radial oscillation. A rough estimate gives that the radial distance between each bunch is 0.1 mm, and as the time between each bunch is 0.025 µs, this results in an approximate radial propagation speed of the oscillations of 4000 m/s.

When these pressure waves reach the boundary of the simulation domain, numerical challenges arise. This is why this report only includes results from the impact of the five first bunches. These challenges have to be studied and understood in order to study the full beam impact.

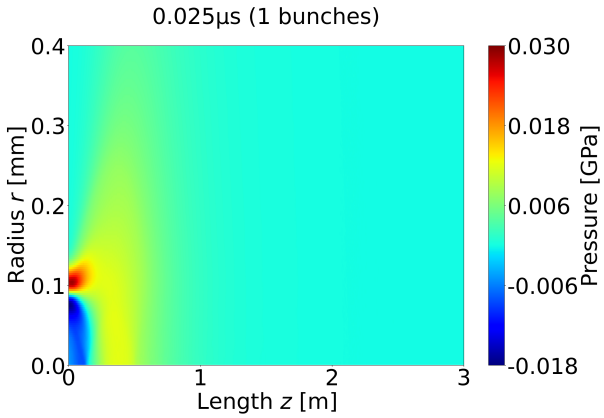

(a) 2D distribution of pressure after the impact of 1 bunch.

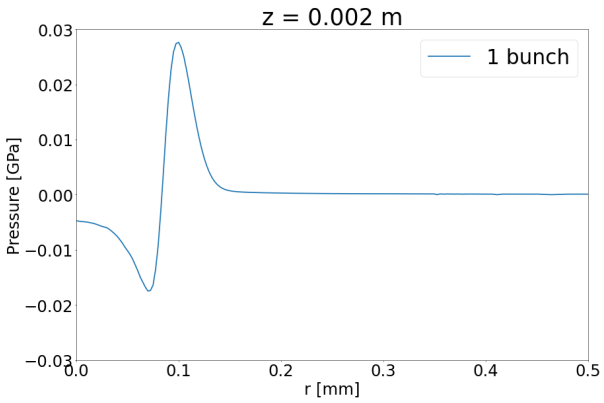

(b) Radial pressure evolution at z = 0.002 m after the impact of 1 bunch.

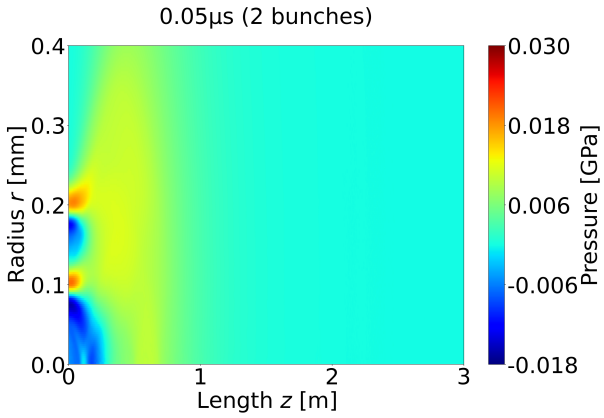

(c) 2D distribution of pressure after the impact of 2 bunches.

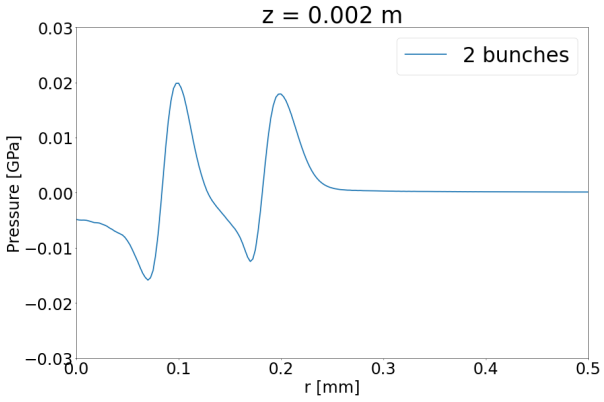

(d) Radial pressure evolution at z = 0.002 m after the impact of 2 bunches.

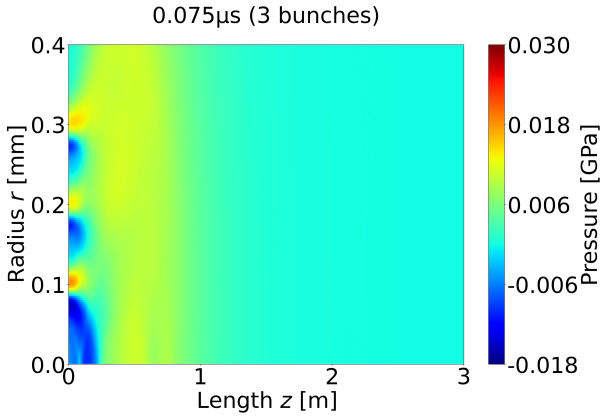

(e) 2D distribution of pressure after the impact of 3 bunches.

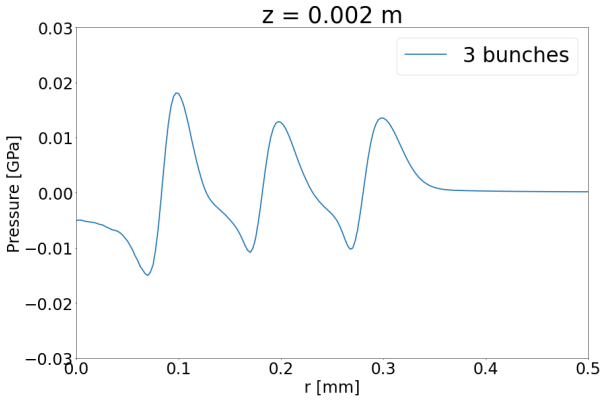

(f) Radial pressure evolution at z = 0.002 m after the impact of 3 bunches.

Figure 5.4.4: 2D distribution of the pressure (a, c, e) and radial evolution at z = 0.002 m (b, d, f) after the impact of 1, 2 and 3 bunches.

Chapter 6

CONCLUSIONS AND OUTLOOK

The assessment of the damage potential of the Future Circular Collider electron/positron (FCC-ee) beams is an important input for the design of the machine protection system. In the Z mode, the beams will operate with 11 200 bunches, each containing 2.14×10^{11} e^-/e^+. This results in a total stored beam energy of 17.5 MJ, which is significantly lower than for both the Large Hadron Collider (LHC) and the High Luminosity LHC (HL-LHC), with stored beam energies of 362 MJ and 681 MJ, respectively. Despite the lower beam energy, the FCC-ee beam introduces unique machine protection challenges due to its highly asymmetric emittance ($\epsilon_x > \epsilon_y$) and the distinct behavior of electron/positron beams, which is expected to affect the characteristics of the energy deposition shower.

In this report, the damage potential of the FCC-ee beam was studied for the Z mode energy and intensity. First, the beam impact was studied for a range of beam sizes. Even if the stored beam energy is significantly lower for the FCC-ee beams than the LHC and HL-LHC beams, results show that the estimated energy density is less different, and the simulated energy deposition has comparable maximum values. For $\beta = 30$ m, the maximum energy deposition of the FCC-ee beam is comparable to the HL-LHC beam. For $\beta = 90$ m, the value is comparable to the LHC beam. When increasing to $\beta = 90$ m, the maximum energy deposition of the FCC-ee beams is considerably lower than both the LHC and HL-LHC beams.

The shape of the energy deposition shower can explain this difference. For FCC-ee, it is much more localized close to the beam impact point compared to the energy deposition shower of the LHC and HL-LHC beams. This is due to the difference in how high-energy electrons and protons interact with the material and the small beam size of the FCC-ee beam in the vertical direction y. The energy deposition curve is very peaked, making it more sensitive to beam size changes than the LHC and HL-LHC beams.

Next, the project presented the initial results for the impact of the first five bunches of the FCC-ee beam simulated with ANSYS Autodyn. Here, the FCC-ee beam was approximated as a round beam with a beam size of 11.5 µm and a bunch intensity of 1.16×10^{10} e^-/e^+. The results showed that the maximum energy deposition scaled to the intensity of one bunch was 317.7 J/g/bunch. This is quite similar to the value obtained from the simulation of the HL-LHC with a beam size of 0.5 mm, which is 294.4 J/g/bunch. When comparing the evolution of density, temperature and pressure for the first five bunches, it was found that the density depletes faster for the impact of the FCC-ee beam

compared to both LHC and HL-LHC. The maximum value for the temperature is very similar for the FCC-ee beam (1332 K) and the HL-LHC beam (1279 K), however the maximum pressure is much lower for the FCC-ee beam than both LHC and HL-LHC.

The density depletion and temperature rise occurred over a significantly more localized region located closer to the beam impact point for the FCC-ee beam compared to the LHC and HL-LHC beams. This could explain why the density depleted so much faster. A key question to understand is how this will keep evolving over time. For the first five bunches, there is almost no longitudinal movement into the material. In order to understand this, a full beam impact study would be required.

BIBLIOGRAPHY

[1] CERN. "The History of CERN". In: *CERN*. World Scientific, 2014. Chap. 1, pp. 1–61. DOI: 10.1142/9789814623476_0001. URL: https://www.worldscientific.com/doi/abs/10.1142/9789814623476_0001.

[2] R. Suarez. "The Future Circular Collider (FCC) at CERN". 2022. arXiv: 2204.10029 [hep-ex]. URL: https://arxiv.org/abs/2204.10029.

[3] R. Schmidt. "Introduction to Machine Protection". In: *CERN Yellow Reports* (2016), Vol 2 (2016): Proceedings of the 2014 Joint International Accelerator School: Beam Loss and Accelerator Protection. DOI: 10.5170/CERN-2016-002.1. URL: https://e-publishing.cern.ch/index.php/CYR/article/view/227.

[4] "FLUKA.CERN website". https://fluka.cern/.

[5] A. Ferrari et al. "FLUKA: a multi-particle transport code". In: *CERN-2005-10 (2005), INFN/TC_05/11, SLAC-R-773* 2005-10 (Jan. 2005). DOI: 10.2172/877507. URL: https://www.osti.gov/biblio/877507.

[6] G. Battistoni et al. "Overview of the FLUKA code". In: *Annals of Nuclear Energy* 82 (2015). Joint International Conference on Supercomputing in Nuclear Applications and Monte Carlo 2013, SNA + MC 2013., pp. 10–18. DOI: https://doi.org/10.1016/j.anucene.2014.11.007.

[7] C. Ahdida et al. "New Capabilities of the FLUKA MultiPurpose Code". In: *Frontiers in Physics* 9 (2022). DOI: 10.3389/fphy.2021.788253.

[8] Ansys Inc. "Ansys Autodyn". https://www.ansys.com/products/structures/ansys-autodyn.

[9] M. Benedikt and F. Zimmermann. "The FCC feasibility study". In: *PoS* EPS-HEP2023 (2023), p. 001. DOI: 10.22323/1.449.0001. URL: https://cds.cern.ch/record/2899894.

[10] O. Brüning et al. *LHC Design Report*. CERN Yellow Reports: Monographs. Geneva: CERN, 2004. DOI: 10.5170/CERN-2004-003-V-1. URL: https://cds.cern.ch/record/782076.

[11] I. Béjar Alonso et al. (Eds.) "High-Luminosity Large Hadron Collider (HL-LHC): Technical design report". In: *CERN-2020-010* (2020), p. 18. DOI: 10.23731/CYRM-2020-0010.

[12] A. Lechner. "Particle interactions with matter". In: *CERN Yellow Rep. School Proc.* 5 (2018), p. 47. DOI: 10.23730/CYRSP-2018-005.47. URL: https://cds.cern.ch/record/2674116.

[13] N. A. Tahir et al. "Impact of high energy high intensity proton beams on targets: Case studies for Super Proton Synchrotron and Large Hadron Collider". In: *Phys. Rev. ST Accel. Beams* 15 (5 May 2012), p. 051003. DOI: 10.1103/PhysRevSTAB.15.051003. URL: https://link.aps.org/doi/10.1103/PhysRevSTAB.15.051003.

[14] F. Burkart. "Expected damage to accelerator equipment due to the impact of the full LHC beam: beam instrumentation, experiments and simulations". Ph.D. Thesis. May 2016. URL: https://cds.cern.ch/record/2229595.

[15] J. Blanco Sancho. "Machine Protection and High Energy Density States in Matter for High Energy Hadron Accelerators". Ph.D. Thesis. 2014. URL: https://cds.cern.ch/record/1704466.

[16] C. Wiesner et al. "Efficient Coupling of Hydrodynamic and Energy-Deposition Codes for Hydrodynamic-Tunnelling Studies on High-Energy Particle Accelerators". In: *Proc. IPAC'21* (Campinas, SP, Brazil). International Particle Accelerator Conference 12. https://doi.org/10.18429/JACoW-IPAC2021-MOPAB024. JACoW Publishing, Geneva, Switzerland, June 2021, MOPAB024, pp. 119–122. ISBN: 978-3-95450-214-1. DOI: 10.18429/JACoW-IPAC2021-MOPAB024. URL: https://accelconf.web.cern.ch/ipac2021/papers/mopab024.pdf.

[17] C. Wiesner et al. "Study of Hydrodynamic-Tunnelling Effects Induced by High-Energy Proton Beams in Graphite". In: *Proc. 13th International Particle Accelerator Conference (IPAC'22)* (Bangkok, Thailand). International Particle Accelerator Conference 13. JACoW Publishing, Geneva, Switzerland, July 2022, WEPOPT015, pp. 1870–1873. ISBN: 978-3-95450-227-1. DOI: 10.18429/JACoW-IPAC2022-WEPOPT015. URL: https://jacow.org/ipac2022/papers/wepopt015.pdf.

[18] J. Don and C. Wiesner. "Simulation of hydrodynamic-tunnelling effects induced by 7 TeV protons in graphite". CERN, Geneva, Switzerland, MPE Technical Note 2022-01, EDMS Nr. 2739903, May. 2022. URL: https://edms.cern.ch/document/2739903.

[19] B. Lindstrom et al. "Fast failures in the LHC and the future high luminosity LHC". In: *Phys. Rev. Accel. Beams* 23.8 (2020), p. 81001. URL: https://journals.aps.org/prab/abstract/10.1103/PhysRevAccelBeams.23.081001.

[20] I.M. Hjelle et al. "Simulated Impact of the HL-LHC Beam on a Graphite Target". In: *Proc. IPAC'24*. International Particle Accelerator Conference 15. https://doi.org/10.18429/JACoW-IPAC2024-MOPC18. JACoW Publishing, Geneva, Switzerland, May 2024, MOPC18, pp. 91–94. ISBN: 978-3-95450-247-9. DOI: 10.18429/JACoW-IPAC2024-MOPC18. URL: https://accelconf.web.cern.ch/ipac2024/pdf/MOPC18.pdf.

[21] J. Kruse-Hansen and C. Wiesner. "Automatic Density Assignment and Generation of FLUKA Input Files for Hydrodynamic-Tunnelling Studies". CERN, Geneva, Switzerland, MPE Technical Note 2021-06, EDMS Nr. 2579002, Apr. 2021. Apr. 2021. URL: https://edms.cern.ch/document/2579002.

[22] I. Kolthoff. "Creating the initial FLUKA model for the hydrodynamic-tunnelling carbon study". 2021. URL: https://gitlab.cern.ch/machine-protection/hydrodynamic-tunnelling/create-initial-fluka-input-lhc-carbon.

[23] The European Strategy Group. *Deliberation document on the 2020 Update of the European Strategy for Particle Physics*. Tech. rep. Geneva, 2020. DOI: 10.17181/ESU2020Deliberation. URL: https://cds.cern.ch/record/2720131.

[24] P. Charitos. "Future Circular Collider - Image selection". In: (2019). General Photo. URL: https://cds.cern.ch/record/2653532.

[25] M. Mangano et al. *FCC Physics Opportunities: Future Circular Collider Conceptual Design Report Volume 1. Future Circular Collider*. Tech. rep. 6. Geneva: CERN, 2019. DOI: 10.1140/epjc/s10052-019-6904-3. URL: https://cds.cern.ch/record/2651294.

[26] I. Efthymiopoulos et al. "HiRadMat: A New Irradiation Facility for Material Testing at CERN". In: CERN-ATS-2011-232 (Nov. 2011). URL: https://cds.cern.ch/record/1403043.

[27] M. Thomson. "Modern Particle Physics". In: 1st ed. Cambridge, UK: Cambridge University Press, 2013. Chap. 1.2, pp. 13–22. ISBN: 9781107034266.

[28] F. Aharonian et al. "High energy astrophysics with ground-based gamma ray detectors". In: *REPORTS ON PROGRESS IN PHYSICS Rep. Prog. Phys* 71 (Sept. 2008), pp. 96901–56. DOI: 10.1088/0034-4885/71/9/096901.

[29] A. Bertarelli. "Beam-Induced Damage Mechanisms and their Calculation". In: (Aug. 2016). DOI: 10.5170/CERN-2016-002.159. URL: https://cds.cern.ch/record/2207167.

[30] A. Fassò, A. Ferrari, and P. R. Sala. "Radiation transport calculations and simulations". In: *Radiation Protection Dosimetry* 137.1-2 (Sept. 2009), pp. 118–133. ISSN: 0144-8420. DOI: 10.1093/rpd/ncp190. eprint: https://academic.oup.com/rpd/article-pdf/137/1-2/118/4532934/ncp190.pdf. URL: https://doi.org/10.1093/rpd/ncp190.

[31] CERN IT Batch Service Documentation. "CERN Batch Service User Guide". https://batchdocs.web.cern.ch/.

[32] A. Piccini and F. Carra. "ANSYS Autodyn Simulations of the Impact of the FCC-ee Beam on Graphite for a Generic Impact Scenario". Private Communication. June 2024.

[33] Y. Nie et al. "Simulation of hydrodynamic tunneling induced by high-energy proton beam in copper by coupling computer codes". In: *Phys. Rev. Accel. Beams* 22 (1 Jan. 2019), p. 014501. DOI: 10.1103/PhysRevAccelBeams.22.014501. URL: https://link.aps.org/doi/10.1103/PhysRevAccelBeams.22.014501.

[34] D. A. Edwards and M. J. Syphers. *An Introduction to the Physics of High Energy Accelerators*. John Wiley & Sons, 2008. ISBN: 978-0-471-55163-8.

[35] T. Wilson. "Introduction to Accelerator Theory". In: Aug. 2011, p. 006. DOI: 10.22323/1.094.0006.

[36] S. Navas et al. "Review of Particle Physics - Particle Data Group". In: *Phys. Rev. D* 110 (Aug. 2024), p. 93. DOI: 10.1103/PhysRevD.110.030001. URL: https://link.aps.org/doi/10.1103/PhysRevD.110.030001.

[37] B. Auchmann et al. "FCC Midterm Report". Unpublished. June 2024.

[38] R.A. Srinivasan M.R. Spiegel J.J. Schiller. *Schaum's Outlines Probabilty and Statistics - Fourth Edition*. The McGraw-Hill Companies, 2013. ISBN: 978-0-07-179558-6.

[39] A. Lechner. "FLUKA Input File for Simulating the Impact of the FCC-ee Beam on Carbon". Private Communication. 13th of May 2024.

[40] V. Vlachoudis. "FLAIR: A Powerful But User Friendly Graphical Interface For FLUKA". In: *Proc. Int. Conf. on Mathematics, Computational Methods, and Reactor Physics (M&C 2009)* (2009).

Appendix A

ADDITIONAL RESULTS FOR THE ROUND FCC-EE BEAM

A.1 Density

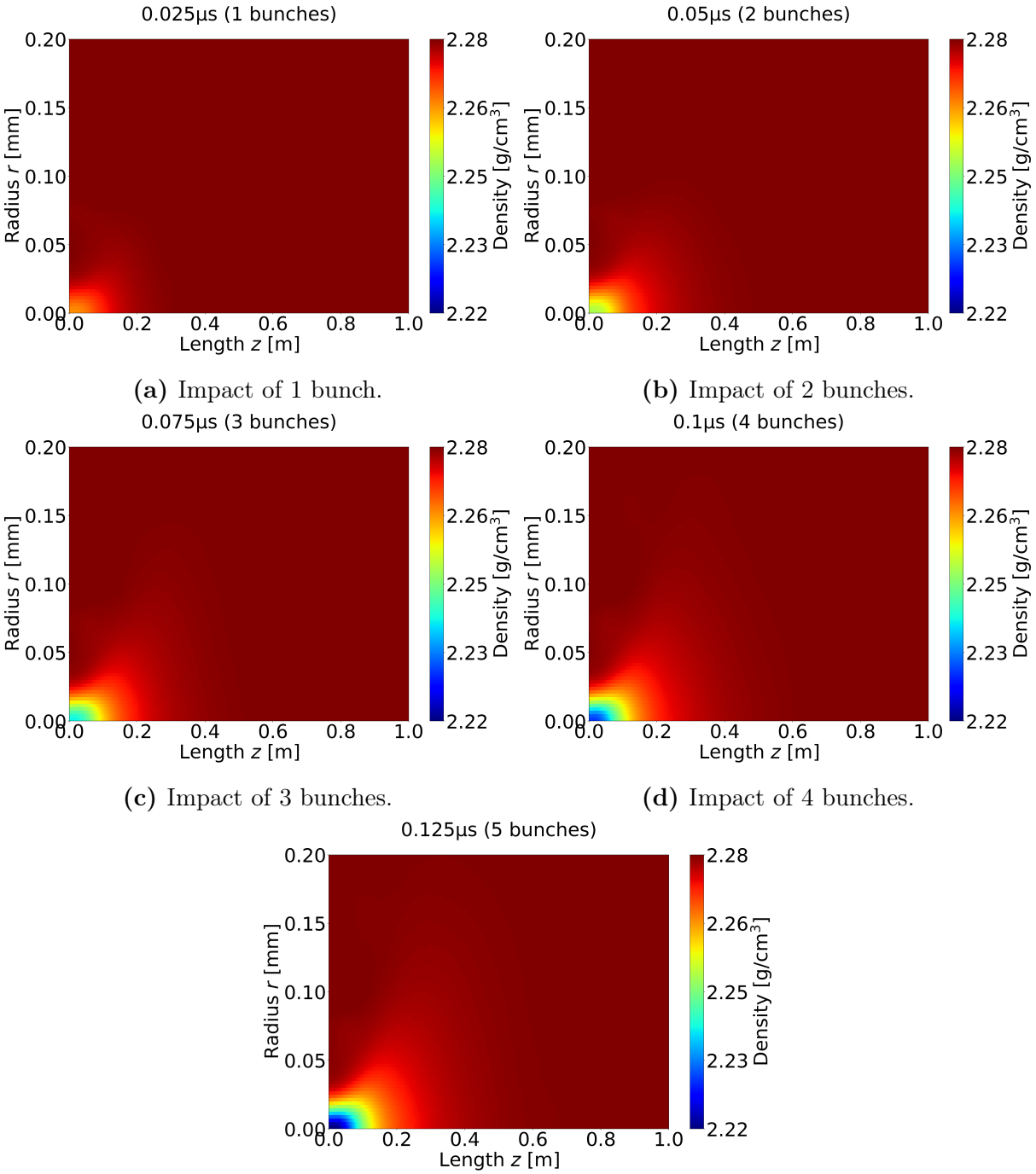

(a) Impact of 1 bunch.

(b) Impact of 2 bunches.

(c) Impact of 3 bunches.

(d) Impact of 4 bunches.

(e) Impact of 5 bunches.

Figure A.1.1: Two dimensional density distribution resulting from the first 5 impacting bunches of the FCC-ee beam scaled to $r = 0.2\,\mathrm{mm}$ and $z = 1\,\mathrm{m}$.

A.2 Temperature

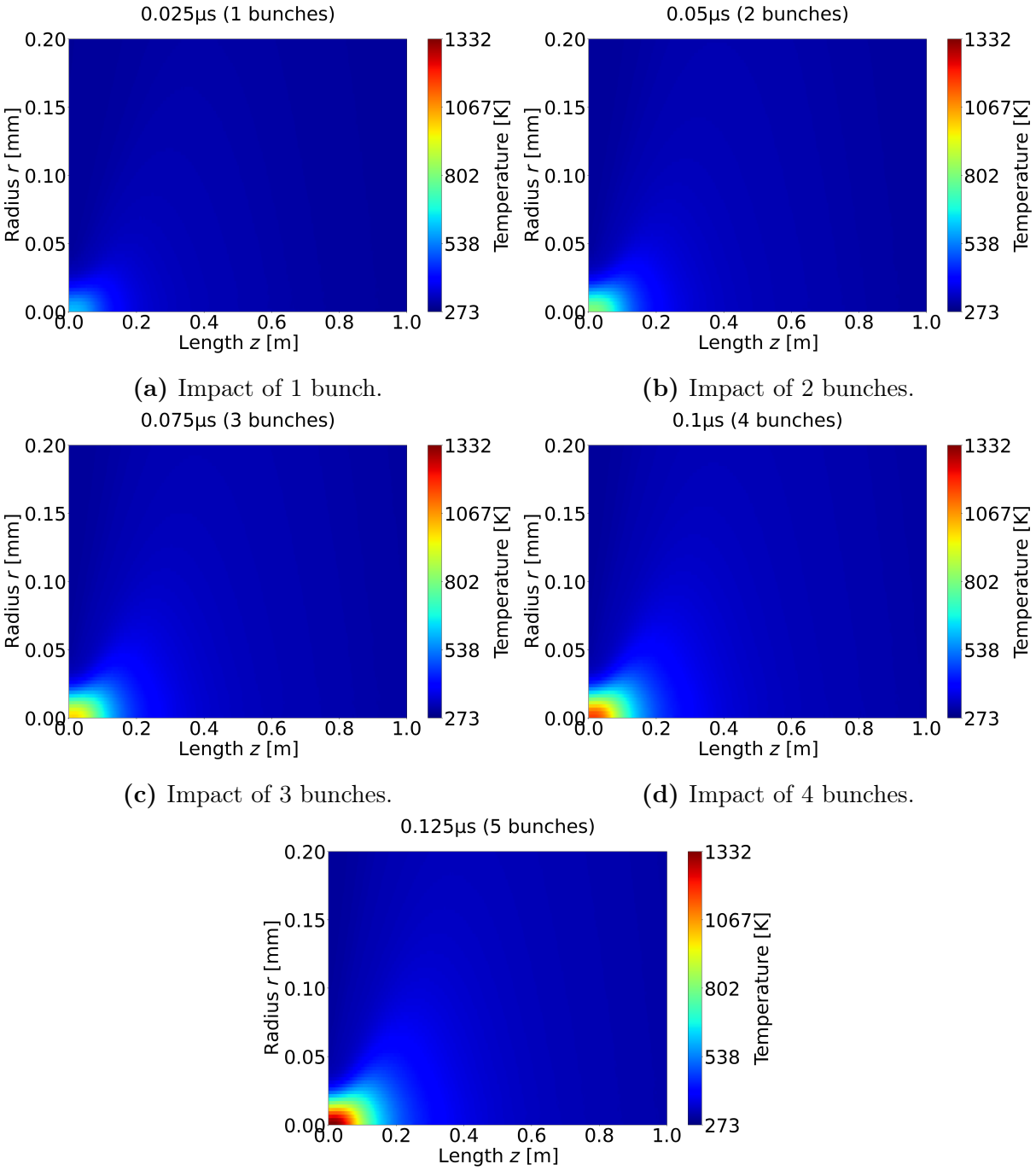

(a) Impact of 1 bunch.

(b) Impact of 2 bunches.

(c) Impact of 3 bunches.

(d) Impact of 4 bunches.

(e) Impact of 5 bunches.

Figure A.2.1: Two dimensional temperature distribution resulting from the first 5 impacting bunches of the FCC-ee beam scaled to $r = 0.2\,\mathrm{mm}$ and $z = 1\,\mathrm{m}$.

A.3 Pressure

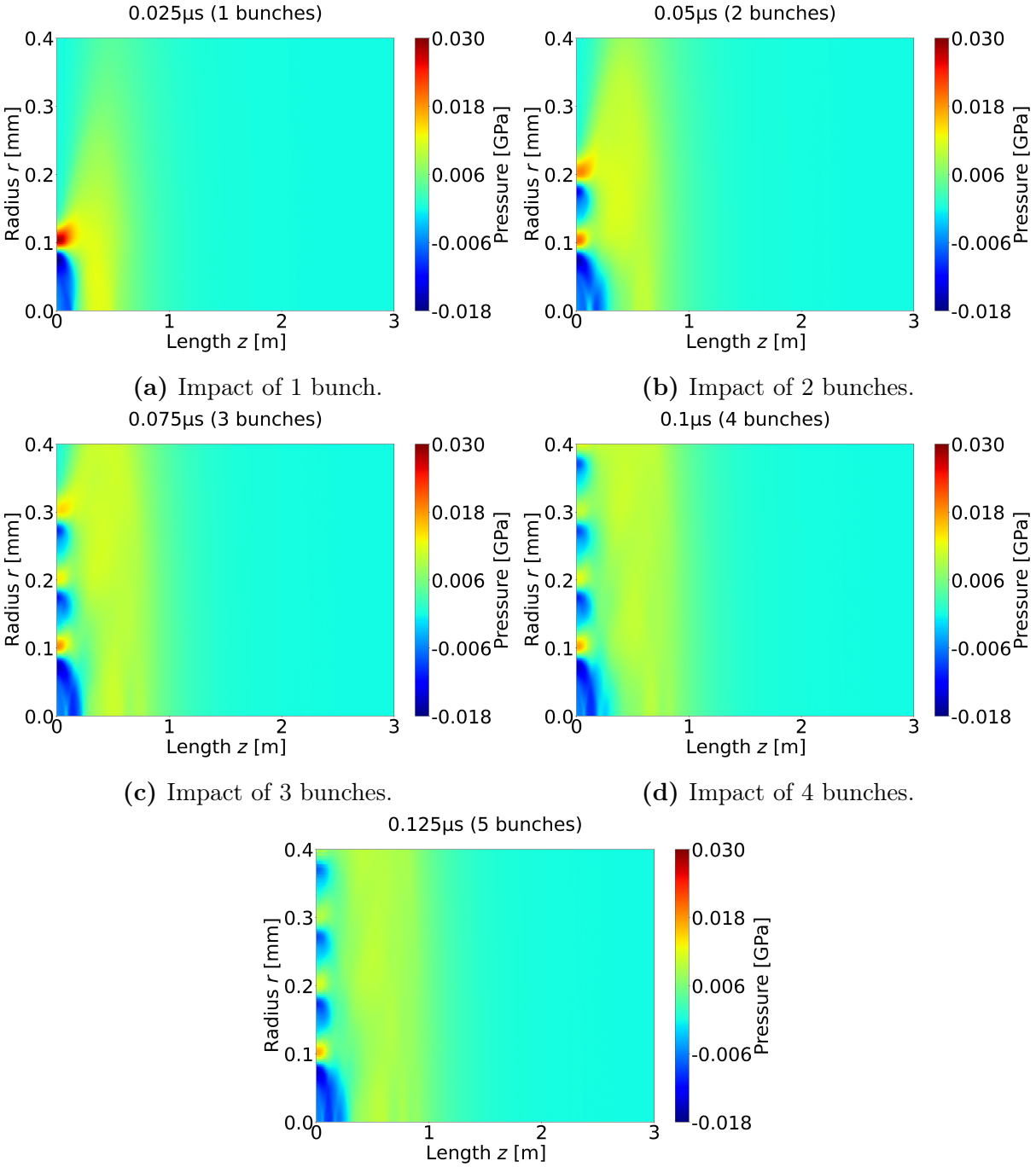

(a) Impact of 1 bunch.

(b) Impact of 2 bunches.

(c) Impact of 3 bunches.

(d) Impact of 4 bunches.

(e) Impact of 5 bunches.

Figure A.3.1: Two dimensional pressure distribution resulting from the first 5 impacting bunches of the FCC-ee beam scaled to $r = 0.4\,\mathrm{mm}$ and $z = 4\,\mathrm{m}$.